2022

Crystalline Analysis of Geomicrobially-Induced Calcium Carbonate Precipitation in Sands using a Surface Percolation Treatment Technique

Justin Edward Mulloney
n01459626@unf.edu

CRYSTALLINE ANALYSIS OF GEOMICROBIALLY-INDUCED CALCIUM CARBONATE PRECIPITATION IN SANDS USING A SURFACE PERCOLATION TREATMENT TECHNIQUE

By

JUSTIN E. MULLONEY

A THESIS PRESENTED TO THE GRADUATE SCHOOL
OF THE UNIVERSITY OF NORTH FLORIDA IN PARTIAL FULFILLMENT
OF THE REQUIREMENTS FOR THE DEGREE OF
MASTER OF SCIENCE

UNIVERSITY OF NORTH FLORIDA

2022

To my family.

ACKNOWLEDGMENTS

Thank you to the professors and staff at the University of North Florida, the Taylor Engineering Research Institute (TERI) and the Biology Department. I would also like to thank Dr. Crowley, Dr. Wingender, and Dr. Ellis on their mentorship, patience, and support. None of this would be possible without the three of you.

TABLE OF CONTENTS

page

LIST OF TABLES

Table page

LIST OF FIGURES

Figure page

Abstract of Thesis Presented to the Graduate School
of the University of North Florida in Partial Fulfillment of the
Requirements for the Degree of Master of Science

CRYSTALINE ANALYSIS OF GEOMICROBIALLY-INDUCED CALCIUM CARBONATE PRECIPITATION IN SANDS USING A SURFACE PERCOLATION TREATMENT TECHNIQUE PRECIPITATION

By

Justin E. Mulloney

May 2022

Chair: Raphael Crowley
Major: Coastal and Port Engineering

Ottawa 50/70 sand specimens and natural beach sand samples were treated using bio-augmented geomicrobies via a surface percolation technique. Testing was conducted on these specimens to determine how resultant calcium carbonate precipitation changed as a function of temperature, depth from the surface, and in the presence of magnesium. Specifically, x-ray Diffraction (XRD), a Scanning Electron Microscope (SEM), and Energy Dispersive X-ray Spectroscopy (EDS) were used to determine and quantify the presence of calcium carbonate and its associated phase. Results showed a direct relationship between temperature and precipitated calcium carbonate. In addition, as an unintended consequence associated with the treatment, ammonium chloride was produced. This ammonium chloride appears to mostly have formed upon the specimens' surfaces, and its quantity appears to be inversely proportional to the quantity of precipitated calcium carbonate. This result has important implications in upscaling in the sense that the results imply that there may be some benefits associated with reducing ammonium chloride precipitation during the microbial reaction. The addition of magnesium led to inconclusive results in the sense that very little calcification was observed during this portion of the study.

CHAPTER 1
INTRODUCTION AND BACKGROUND

1.1 Erodibility of Dunes, Beachheads, and the Intracoastal Waterway

In the state of Florida, a "critically eroded shoreline" is defined as a shoreline that has eroded or recessed to a point where resources, development, or habitats are degraded or lost. The 2021 Florida Department of Environmental Protection (FDEP) on critically eroded shoreline lists 688 km of critically eroded beach, 146 km of critically eroded inlet shoreline, 143 km of non-critically eroded beach and 5.1 km of non-critically eroded inlet (FDEP 2021). The overall length of critically eroded beaches and critically eroded length along inlets has increased 11 km and 0.8 km respectively since 2019. Increasing the erosion resistance of dunes, shorelines, and inlets is crucial in sustaining Florida's shorelines.

1.2 Microbially Induced Calcite Precipitation Overview

In recent years, much literature has shown that microbially-induced calcite precipitation (MICP) may be a new, sustainable, environmentally friendly soil stabilization technique when compared with other, more traditional soil improvement techniques (see DeJong et al. 2010 or Krajewska 2018 for example).

As summarized by Chek et al.(2021), MICP is initiated via urea hydrolysis which results in the formation of ammonium and carbamic acid:

$$CO(NH_2)_2 + H_2O \rightarrow NH_2COOH + NH_3 \quad (1\text{-}1)$$

Carbamic acid then hydrolyzes to ammonia and carbonic acid:

$$NH_2COOH + H_2O \rightarrow NH_3 + H_2CO_3 \quad (1\text{-}2)$$

The by-products of Eq. (1-2) balance in water to form ammonium, bicarbonate, and hydroxide ions that raise the pH:

$$H_2CO_3 \leftrightarrow HCO_3^- + H^+ \quad (1\text{-}3)$$

$$2NH_3 + 2H_2O \leftrightarrow 2NH_4^+ + 2OH^- \quad (1\text{-}4)$$

The pH increase tends to shift bicarbonate equilibrium and produce carbonate ions:

$$HCO_3^- + H^+ + 2OH^- \leftrightarrow CO_3^{2-} + 2H_2O \quad (1\text{-}5)$$

Lastly, calcium carbonate precipitation occurs at the bacterial cell surface when there is a sufficient concentration of calcium and carbonate ions in the solution (Dejong et al., 2006):

$$Ca^{2+} + Bacterial\ Cell \leftrightarrow Cell - Ca^{2+} \quad (1\text{-}6)$$

$$Cell - Ca^{2+}CO_3^{2-} \rightarrow Cell - CaC0_3 \quad (1\text{-}7)$$

1.3 Calcium Carbonate Process Control

Calcium carbonate ($CaCO_3$) minerals form different rock-types found geologically including limestone, chalk, and marble. $CaCO_3$ has three anhydrous crystalline polymorphs: calcite, aragonite, and vaterite. Calcite is the most thermodynamically stable, followed by aragonite and vaterite (Morse et al., 2007). The most common polymorph is calcite, which has a rhombohedral shape, followed by aragonite which has a needle-like shape, and finally vaterite which is spherical in shape. Krajewska (2018) noted that when using *Sporosarcina pasteurii* to initiate the MICP process (i.e., Eq. 1-1 through Eq. 1-7), calcite is primarily obtained.

However, in recent years, several researchers have pointed out that there may be advantages to precipitating aragonite as opposed to calcite because aragonite's interlocking needle-like crystals appear to lead to improved strength increases when compared to situations where mostly calcite is precipitated. Uddin (2020) noted cement pastes that transform to aragonite possess 10 times higher compressive strengths than cement pastes comprised exclusively of calcite. Likewise, Zhang et al. (2015) stated that improved strength of microbial mortar may be related to the precipitation of aragonite. Heriansyah et al. (2016) also concluded that the presence of aragonite during enzyme-induced calcite precipitation (EICP) improved the unconfined

compressive strength (UCS) of treated samples when compared to specimens where mostly calcite had been precipitated. Hargis et al. (2021) showed that when vaterite converts to aragonite, a strength increase of almost 40 MPa could be achieved, and this was attributed to aragonite's needle-like arrangement.

1.4 Addition of Magnesium

To induce aragonite precipitation, most previous studies introduced some Mg^{2+} to the reaction in Eq. 1-6 – either via substitution with Ca^{2+} or as an additive. For example, Heriansyah et al. (2016) substituted 0.05 Molar (M) to 0.25 M Mg^{2+} in Eq. 1-6 and via testing with acid washing, x-ray diffraction (XRD), and a scanning electron microscope (SEM) attributed their increases in overall $CaCO_3$ precipitation, aragonite precipitation, and UCS to the addition of Mg^{2+}. Charndra et al. (2020) similarly substituted Mg^{2+} during an EICP study and XRD data showed apparent increases in aragonite and vaterite precipitation along with concomitant increases in UCS. Xu et al. (2020) showed that using 0.01 M Mg^{2+} solution in conjunction with $CaCH_3COO_2$ and urea resulted in increases in UCS, and that increasing the concentration of Mg^{2+} led to even higher UCS improvements.

1.5 MICP Treatment for Erosion Mitigation

Traditionally, most studies involving EICP and MICP concentrated on demonstrating strength improvements associated with treatment. But, as pointed out by Mehta (1991), strength improvements do not necessarily directly correlate to improvements in erosion resistance. More recently however, several researchers have begun exploring EICP/MICP in the context of improved erosion resistance. Salifu et al. (2016) showed that MICP treated sand was significantly more erosion-resistant when compared to untreated sand during simulated tidal cycling. Similarly, Wang et al. (2020) showed that embankments treated with MICP eroded less under simulated rainfall conditions than untreated embankments. Do et al. (2020) investigated using MICP for

structural scour mitigation and showed that structures with treated sand eroded significantly less than untreated specimens. Saracho et al. (2021) used an erosion function apparatus (EFA; Briaud et al. 2001) to quantify erosion improvement associated with MICP treatment and noted an indirect relationship between calcification and erodibility. Finally, Liu (2021) tested small-scale dunes under water wave attack in a wave tank. Results showed that, in general, treated dunes were more erosion resistant. Most recently, Chek et al. (2021) used a pocket erodometer (Briaud et al. 2011) to quantify MICP-treated specimen erodibility. Results showed that treated specimens eroded significantly less than untreated specimens and that increases in bacterial optical density, calcium, and urea tended to correlate indirectly with erodibility. In all known cases, during these previous erosion studies, bio-augmented MICP treatment was used.

Overall, the increasing body of literature appears to suggest that eventually MICP/EICP may be effective for erosion mitigation and could potentially be used in conjunction with or partially replace current coastal "standard" mitigation strategies like riprap or bulkhead placement that are known to have their own sets of environmental issues (Chek et al. 2021). However, the current body of literature has mostly focused on using EICP/MICP via column and/or soil injection. As noted in the introduction, hundreds of miles of Florida's coastline are critically eroded. Using a column injection method on length scales of this magnitude may not be feasible. However, two of the recent studies – Liu et al. (2021) and Chek et al. (2021) utilized a surface percolation treatment technique whereby relatively high concentrations of bacteria, $CaCl_2$, and urea were applied to the surface and allowed to percolate through their soils. Over large length scales like the ones described in this paper's introduction, this technique would appear to be feasible for upscaling.

1.6 Knowledge Gaps

What remains unclear from both the Liu et al. (2021) and Chek et al. (2021) studies are the morphological properties associated with calcium precipitation as a function of depth when a surface percolation treatment technique is used. This is important because morphology, such as the needle-like morphology of aragonite, is dictated by the phase/polymorph, which this investigation hypothesizes can be controlled with the addition of magnesium ions. Both Liu et al. (2021) and Chek et al. (2021) focused on erosion alone as their metric for success associated with treatment. While Chek et al. (2021) performed some XRD analyses, these analyses were confined to specimens from their sample surfaces. Mineral production and polymorph-types as a function of depth were not quantified, and one would expect mineral production to decrease as a function of depth because of natural diffusion gradients. Furthermore, as noted, a limited number of studies have been conducted where Mg^{2+} was added to the MICP recipe. But, yet again, these previous efforts were conducted using column/injection techniques, and, as such, it was unclear if specimens treated via surface percolation would have similarity.

Lastly, both the Chek et al. (2021) and Liu et al. (2021) studies were similar in the sense that after treatment, their specimens were held at a constant temperature prior to erosion testing. During a summer day in Florida, temperatures may range from 30°C to 50°C (NOAA, 2022). While others have studied temperature, ranging from 10°C to 30°C, effects associated with MICP treatment (Achal 2019 for example, there are many other similar studies), these previous studies almost exclusively utilized column/injection treatment techniques. It was unclear if specimens treated via surface percolation would behave similarly.

1.7 Goals and Objectives

This study's goal was to fill these knowledge gaps. Specifically, this study's goals were as follows:

1. To determine how CaCO3 formation varies as a function of post-treatment temperature when sand specimens are treated via MICP and a surface percolation treatment technique.
2. To determine how CaCO3 formation varies as a function of depth when sand specimens are treated via MICP and a surface percolation technique.
3. To determine how the addition of Mg2+ may alter the CaCO3 phase when sand specimens are treated via MICP and a surface percolation treatment technique.

Like previous studies, investigators sought to answer these questions using bio-augmented (as opposed to bio-stimulated) techniques. While many previous studies used acid washing to quantify calcification (Choi et al. 2017), Chek et al. (2021) pointed out issues with this approach for unsaturated specimens. When specimens dehydrate, they tend to leave behind precipitated salts, particularly ammonium chloride, calcium chloride, and in some cases (if native beach sand is used), sodium chloride. During acid wash testing, these residual salts will be washed away along with the $CaCO_3$. Thus, as Chek et al. (2021) discuss, the difference in mass of a desaturated specimen before and after an acid wash test does not represent the amount of precipitated calcium carbonate. As such, this study exclusively utilized X-ray diffraction (XRD) in conjunction with scanning electron microscopy (SEM) and energy dispersive spectroscopy (EDS) to examine the crystallographic nature of $CaCO_3$ MICP reaction products.

It was hypothesized that with an increase of temperature there will be an increase in $CaCO_3$ formation, and that the addition of Mg^{2+} would shift the $CaCO_3$ preferred phase to aragonite. Finally, investigators hypothesized that $CaCO_3$ precipitation would decrease as a function of depth when the surface percolation treatment technique was used.

CHAPTER 2
METHODOLOGY

2.1 Sediment Characteristics

Two types of MICP substrates were used throughout this study. First, following Chek et al. (2021), beach sand from Atlantic Beach, FL was used. The advantage to this approach is that it allows one to understand $CaCO_3$ precipitation under more natural conditions, but the disadvantage to this approach is that beach sand may contain intrinsic $CaCO_3$ phases present from local shells and corals that might confound analysis. To better understand the reaction products of this complex system, a control substrate of pure quartz, 50/70 Ottawa sand was used in addition to native beach sand.

The beach sand consisted of archived material from the Chek et al. (2021) study where it was reported that this soil was classified as poorly graded sand, i.e., SP according to the Unified Soil Classification System (Chek 2019). The void ratio and porosity were reported as 0.36 and 0.26 respectively (Chek 2019). The Ottawa 50/70 sand was classified as poorly graded ie. SP, according to the Unified Soil Classification System. ATSM D854 (2014) was used to find the void ratio and porosity of both reaction substrates. The void ratio and porosity were 0.77 and 0.43 respectively. The grain size distributions associated with the beach sand and Ottawa sand are shown below in Fig. 2-1:

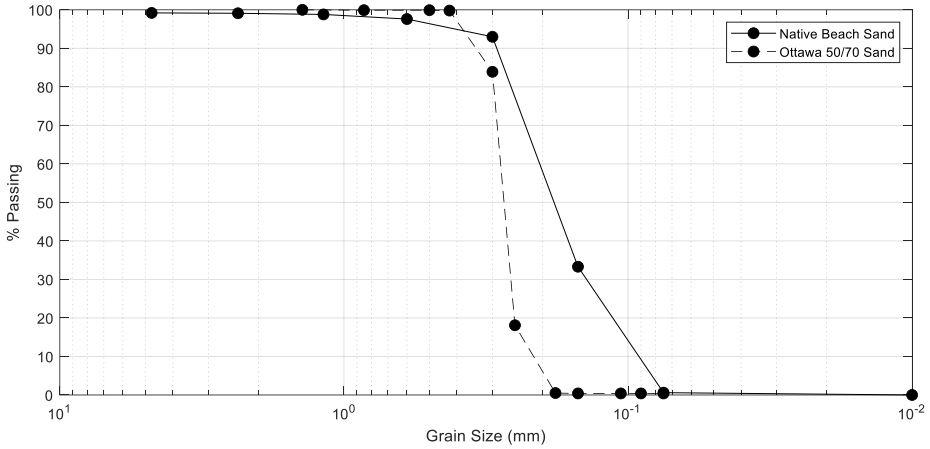

Fig. 2-1: Grain Size Distribution for Native Beach Sand and Ottawa 50/70 Sand shows both substrates are classified as poorly graded by the Unified Soil Classification System.

2.2 Specimen Preparation

Several testing tubes were prepared by air pluviating 1,300 g of sand into 10.1 cm diameter by 20 cm high standard concrete tubes. Prior to pluviation, several orifices were punched through the tubes' bottoms to allow fluid to drain through the tubes and the bottoms of tubes were covered with premium landscape fabric to prevent soil from leaking through the orifices. Once filled, the height of each specimen was approximately 10.2 cm for the beach sand, and 10.0 cm for the Ottawa 50/70 sand. Eq. 2-1 below was used to compute the void volume, V_v, associated with each specimen:

$$V_v = \frac{V_T e}{1+e} \tag{2-1}$$

The total V_v was 216 ml per specimen for the beach sand and 344 ml per specimen for the Ottawa 50/70 sand. Volume of the voids for each substrate was the determining factor in the treatment volume of MICP solution.

2.3 MICP Constituent Preparation

Following Chek et al. (2021), *S. pasteurii* NRS2929 (USDA) were grown overnight from 1 ml frozen glycerol stocks on Brain Heart Infusion (BHI) agar plates and 2% urea at 30 °C. Cells

were then scraped from the plates to inoculate liquid cultures of Brain Heart Infusion broth and 2% urea. Liquid cultures (1-2 liters) were grown overnight in Fernbach flasks at 30 °C and 200 rpm for continuous aeration using a shaker incubator. Liquid *S. pasteurii* cultures were grown to an optical density (OD) of 3.0 for all experiments. An Eppendorf BioPhotometer plus Model 6132 spectrometer was used to measure the OD at a wavelength of 600 nm prior to each application.

Calcium and urea were prepared by mixing a solution of 2.5-M urea and 2.5-M $CaCl_2$. When magnesium was used, $MgCl_2$ was added to the urea/$CaCl_2$ solution in varying quantities that will be described below.

2.4 XRD, SEM, and EDS Testing

All XRD testing was conducted using the University of North Florida (UNF) Materials Science and Engineering Research Facility (MSERF) Shimadzu XRD 6100 diffractometer (Kyoto, Japan) at 40 kV and 30 mA using a scan speed of 2°/min and a step size of 0.02° over a 2Θ range of 20° to 65°. The phase identification of the specimens was determined by via Bragg angle analysis by comparing result from the XRD with known Bragg angles from the International Centre for Diffraction Data (ICDD) software Powder Diffraction File (PDF) – 4+ (ICDD 2021).

SEM testing was conducted using the UNF MSERF Tescan Vega 3 Scanning Electron Microscope. The Vega 3 has a tungsten source, and an accelerating voltage of 15 kV. Sand samples were mounted on aluminum SEM stubs using conductive carbon tape and then sputter coated with gold (Au), using a Cressington sputter coater, to enhance conductivity. Energy Dispersive X-ray Spectroscopy (EDS) was completed to help better understand the elements present in the SEM images. EDS was performed using an Oxford Ultim Max 65 detector. Elemental maps were generated with Oxford's Aztec Software (Version 5.1.7829, 2021).

2.5 Treatment Techniques and Test-Series

Three test-series were conducted during this investigation. All test-series utilized the surface percolation technique referenced in Chapter 1. In general, results from Chek et al. (2021) showed that calcium carbonate precipitation after surface percolation treatment was maximized (and erodibility was minimized) when 100% of specimens V_v or pore volume (PV) were filled with fluid using a 1:1 ratio between bacterial broth and cementation solution (i.e., urea/calcium chloride, etc.). As such, during treatment, a volume of bacterial broth corresponding to approximately 50% of the specimens' PV was applied to the surfaces directly at a flow rate of approximately 50 ml/s. Immediately thereafter, a volume of cementation solution corresponding to 50% of the specimens' PVs was applied to the specimens' surfaces at approximately the same rate. The sample tubes were then allowed left undisturbed for 48 hours at approximately 20°C.

2.5.1 Temperature Study

The first test-series involved investigating how temperature affected $CaCO_3$ production. To assess this, after the initial 48-hour room temperature cure, samples were dried for an additional 96 hours at varying temperatures ranging from 20°C to 50°C. This was meant to simulate potential temperatures that could be encountered along a shoreline during typical summer months in Florida. Then, specimens were obtained from the samples' surfaces and subjected to XRD, SEM, and EDS testing. A table that illustrates the tests that were performed during this test-series is shown below in Table 2-1. As shown, both beach and Ottawa sand were used during this portion of the study.

Table 2-1: Testing Matrix for the Temperature Study

Test	Sand Type	Cementation Solution	Cure Temperature (°C)
T1	Ottawa 50/70	2.5 M Urea / 2.5 M $CaCl_2$	20
T2	Ottawa 50/70	2.5 M Urea / 2.5 M $CaCl_2$	30
T3	Ottawa 50/70	2.5 M Urea / 2.5 M $CaCl_2$	50
T4	Native Beach Sand	2.5 M Urea / 2.5 M $CaCl_2$	20
T5	Native Beach Sand	2.5 M Urea / 2.5 M $CaCl_2$	30
T6	Native Beach Sand	2.5 M Urea / 2.5 M $CaCl_2$	50

2.5.2 Depth Study

The second test-series was designed to determine how or if $CaCO_3$ production varied as a function of depth when a topical surface percolation technique was used. During this test-series, after the initial 48-hour cure, specimens were placed in an oven at 100°C for 96 hours. Then, specimens were taken from the center of cured samples at 20-mm increments and subjected to XRD, SEM, and EDS analysis. A table that illustrates the tests that were conducted during this test-series is shown below in Table 2-2. As shown, only beach sand was used during this portion of the study.

Table 2-2: Testing Matrix for the Depth Study

Test	Sand Type	Cementation Solution	Cure Temperature (°C)	Depth from Surface (cm)
D1	Native Beach Sand	2.5 M Urea / 2.5 M $CaCl_2$	100	0-2
D2	Native Beach Sand	2.5 M Urea / 2.5 M $CaCl_2$	100	2-4
D3	Native Beach Sand	2.5 M Urea / 2.5 M $CaCl_2$	100	4-6
D4	Native Beach Sand	2.5 M Urea / 2.5 M $CaCl_2$	100	6-8
D5	Native Beach Sand	2.5 M Urea / 2.5 M $CaCl_2$	100	8-10

2.5.3 Addition of Magnesium

The final test-series was to preliminarily investigate the effect of magnesium on the $CaCO_3$ precipitation process. During this study, during cementation solution preparation, quantities of $MgCl_2$ were added to the urea/$CaCl_2$ solution prior to treatment. Table 2-3 below illustrates the tests that were conducted during this portion of the study. After the initial room-temperature cure, these specimens were subjected to an additional cure at 30°C for 96 hours. Then, surface specimens were obtained from the sample surfaces and subjected to SEM, XRD, and EDS testing.

Table 2-3: Testing Matrix for the Magnesium Study

Test	Sand Type	Cementation Solution	Magnesium	Cure Temperature (°C)
Mg1	Native Beach Sand	2.5 M Urea / 2.5 M $CaCl_2$	0.5 M	30
Mg2	Native Beach Sand	2.5 M Urea / 2.5 M $CaCl_2$	1.0 M	30
Mg3	Native Beach Sand	2.5 M Urea / 2.5 M $CaCl_2$	2.5 M	30
Mg4	Ottawa 50/70	2.5 M Urea / 2.5 M $CaCl_2$	0.5 M	30
Mg5	Ottawa 50/70	2.5 M Urea / 2.5 M $CaCl_2$	1.0 M	30
Mg6	Ottawa 50/70	2.5 M Urea / 2.5 M $CaCl_2$	2.5 M	30
Mg7	Ottawa 50/70	N/A	2.5 M	30

2.5.4 Control Testing

Finally, several control (i.e., untreated) specimens were tested using XRD, SEM, and EDS.

2.6 XRD Paremeters

Jian et al. (2003) showed that an XRD-associated peak may be analyzed using 5 basic parameters: peak location, full-width at half maximum (FWHM), maximum intensity, shape, and symmetry. This investigation focuses on peak location, FWHM, and peak intensity.

2.6.1 Peak Location

Diffraction peaks position may be described by Bragg's Law:

$$\lambda = 2dsin\theta \quad (2\text{-}2)$$

where the x-ray wavelength is fixed and represented by λ; the distance between parallel planes of atoms is d; and the peak location, or Bragg angle, is θ. For a parallel plane of atoms, with a space, d, diffraction occurs when Bragg's Law is satisfied. Diffraction for a given set of crystallographic planes, as defined by Miller Indices, can occur at a given Bragg angle. Thus, XRD can be used for phase identification as well as semiqualitative analyses using the aforementioned parameters obtained from peak fitting.

2.6.2 Full-Width at Half Maximum and Peak Intensity

The shape and intensity of a diffraction peak can be used to describe the crystalline phases using several parameters obtained from fitting a model to the empirical data that can be interpreted using the Scherrer equation:

$$\beta = \frac{\mathrm{K}\,\lambda}{\tau cos\theta} \quad (2\text{-}3)$$

This equation relates the size of crystallites to a broadening of their peaks in a diffraction pattern. The broadening, or width, of a peak in a diffraction pattern is measured at half of the maximum intensity, or full-width at half maximum (FWHM). In this equation, FWHM is represented by β; K is a dimensionless shape factor that varies with the shape of the crystallite; and the mean size of crystalline domains is τ. Thus, this equation inversely relates peak width to crystallite size. The constraint on the Sherrer Equation is that it is not applicable to grains larger than 0.1 to 0.2 μm. There are also a variety of other factors that can affect peak broadening including strain and crystal lattice imperfections.

Peak intensity reflects both absorbance and amount of phase in the mixture (Jian et al., 2003). Peak intensity can also be described by the Laue Equations and may indicate relative phase

fraction analysis when comparing peak heights for the same Bragg Angles across two different samples.

2.7 Data Analysis

To analyze XRD data, four parameters were studied: peak locations, relative intensity, integrated area, and FWHM. The steps to analyze data are below.

1. A baseline correction was conducted in Fityk (version 1.3.1, 2016) using raw data (see Fig. 3-1 below) to account for instrument/background noise.

2. Data were then imported into Microsoft Excel 2016 (Microsoft 2016) where data were normalized relative to control substrate quartz peaks. After performing baseline correction and normalization, a subtraction process was performed to remove spectral intensity associated with the substrate to improve visualization of MICP $CaCO_3$ phases and fit a model to empirical data.

3. Data from this process were imported back into Fityk where curve fitting was conducted to back-solve for the precipates of interest.

Peak locations of interest and their associated minerals and Miller Indices are summarized below in Table 2-4:

Table 2-4: Peak Locations and Associated Crystals

Crystal	Peak Location (Degrees) and Miller Indices
Vaterite	24.90 (110)
Calcite	29.40 (104)
Sodium Chloride	31.69 (200)
Ammonium Chloride	32.65 (110)
Aragonite	33.12 (012)
Calcium Chloride	38.59 (211)

Peak locations were used to infer whether these minerals had been produced. FWHM results were used to qualitatively describe the atomic disorder of crystalline phases which may reflect the speed

of formation, or reaction kinetics. The peak intensities and areas under the diffraction curves were used to approximate the relative amounts of precipitate in each specimen.

SEM images were used to visually confirm precipitate formation and its location. Elemental maps were generated using EDS to show overlap of various elements and where they may have co-precipitated. If, for example, EDS data showed that calcium, carbon, and oxygen were present in the same region in a specimen, and XRD data showed peaks associated with a calcium carbonate polymorph, these data taken together suggest that calcium carbonate had been produced at these locations.

CHAPTER 3
RESULTS

3.1 Temperature Study

Results from the Temperature Study are presented below in Fig. 3-1 through Fig. 3-4.

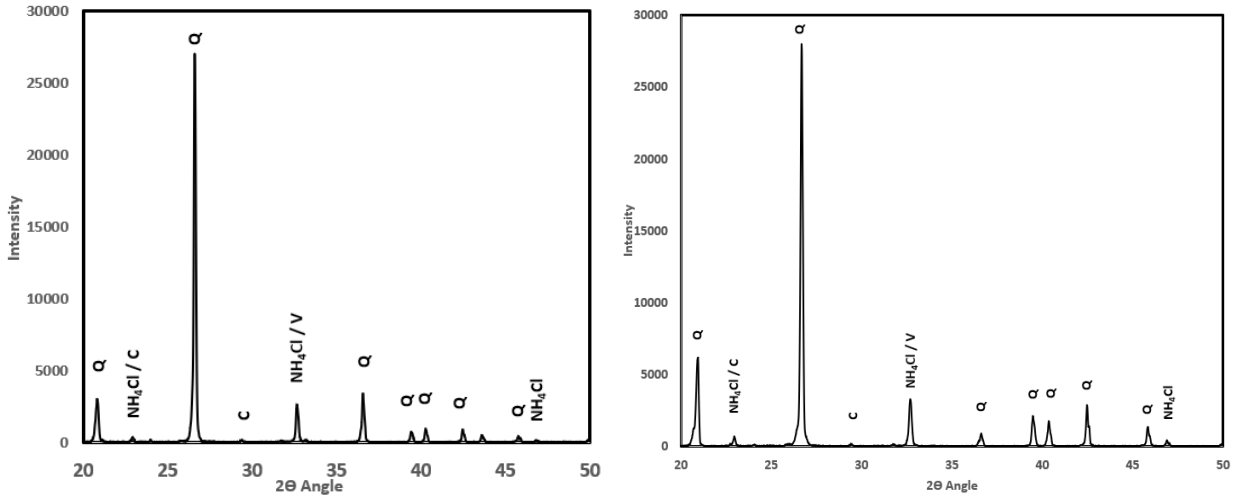

(a) (b)

Fig. 3-1: Diffracted intensities and corresponding minerals at each angle for (a) T6 - treated native sand, cured at 50°C and, (b) T3 - treated Ottawa Sand, cured at 50°C.

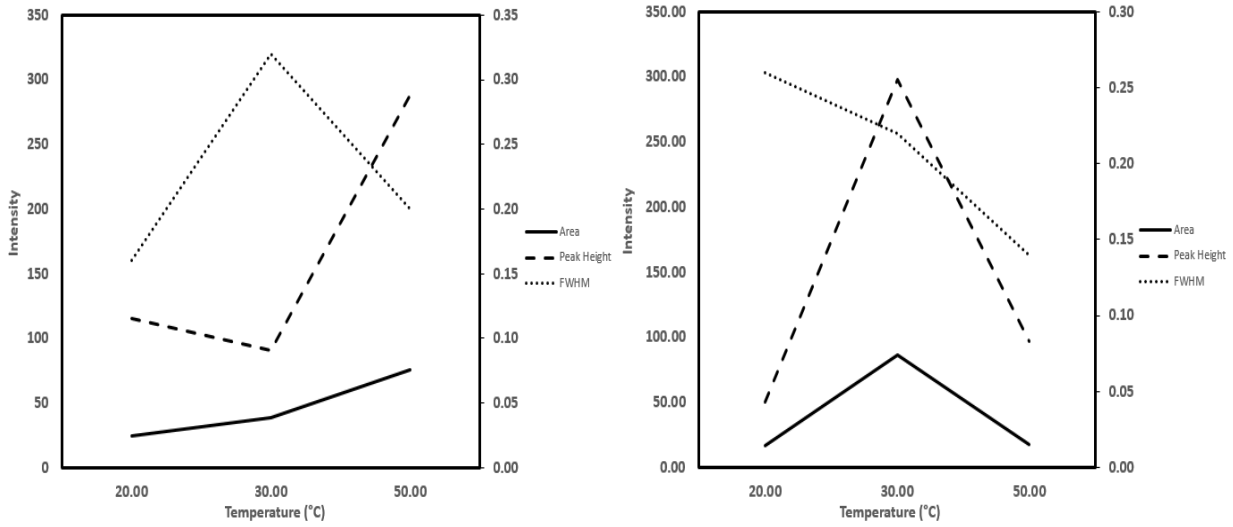

(a) (b)

Fig. 3-2: Area, peak height, and full width-half maximum of the prominent $CaCO_3$ peak at 29.40° over a range of temperatures. (a) shows data for treated native beach sand and (b) shows data for treated Ottawa 50/70 sand.

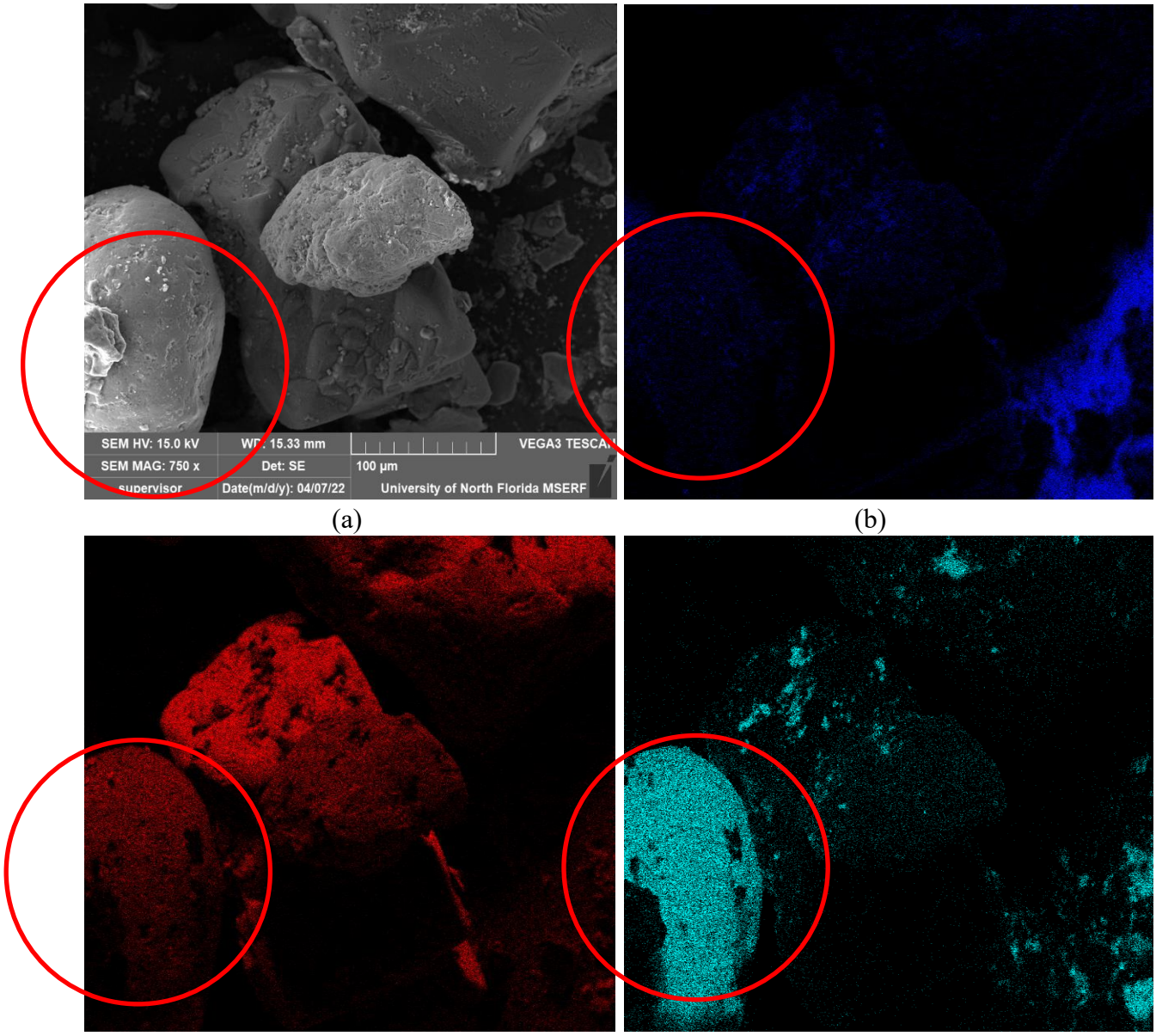

(a) (b)

(c) (d)

Fig. 3-3: SEM and EDS images from T5 - treated beach sand, cured 30°C. (a) SEM image, (b) Carbon readings from EDS, (c) Oxygen readings from EDS, (d) Calcium readings from EDS.

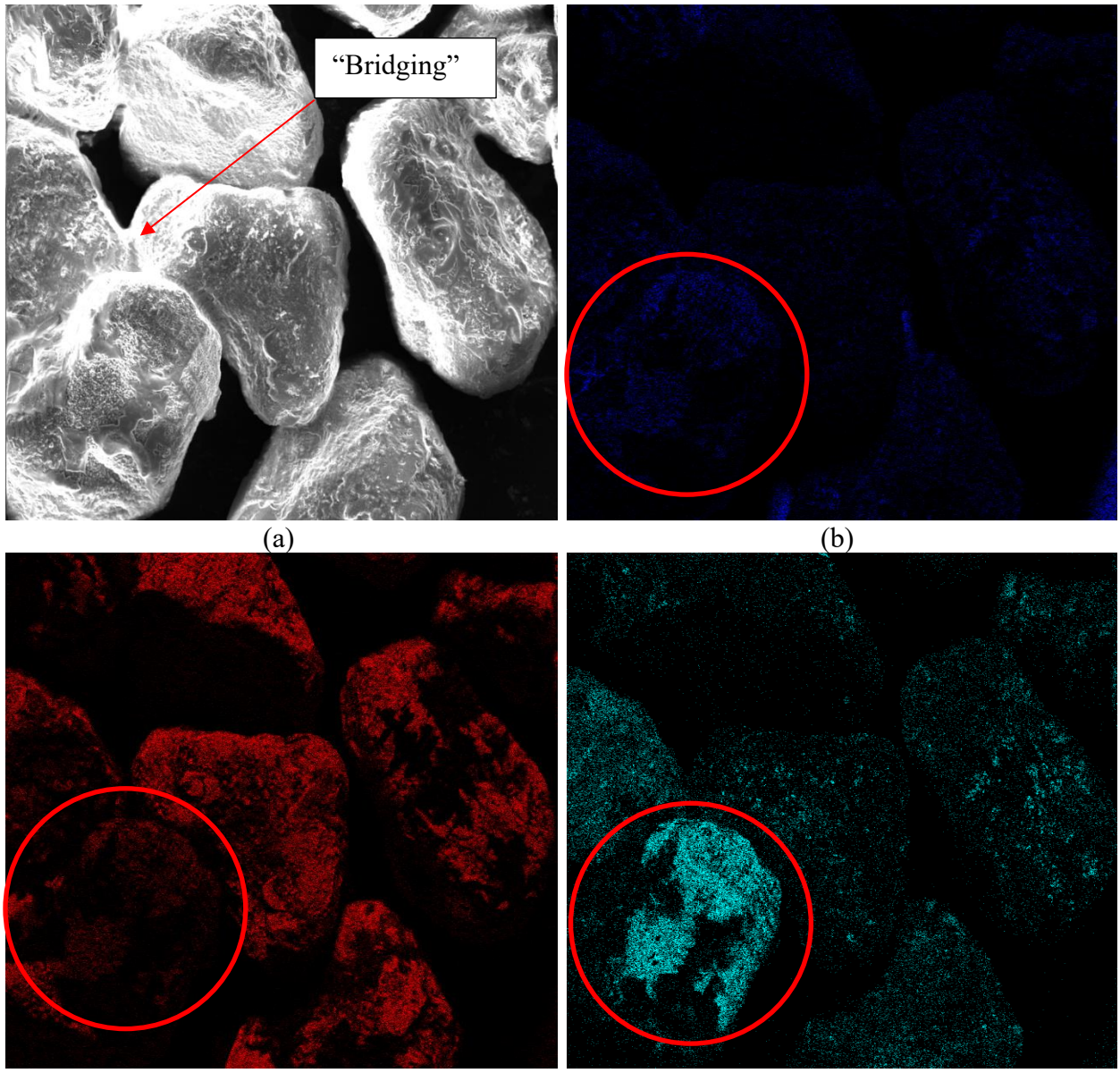

Fig. 3-4: SEM and EDS images from T2 - treated Ottawa 50/70 sand, cured 30°C. (a) SEM image, (b) Carbon readings from EDS, (c) Oxygen readings from EDS, (d) Calcium readings from EDS.

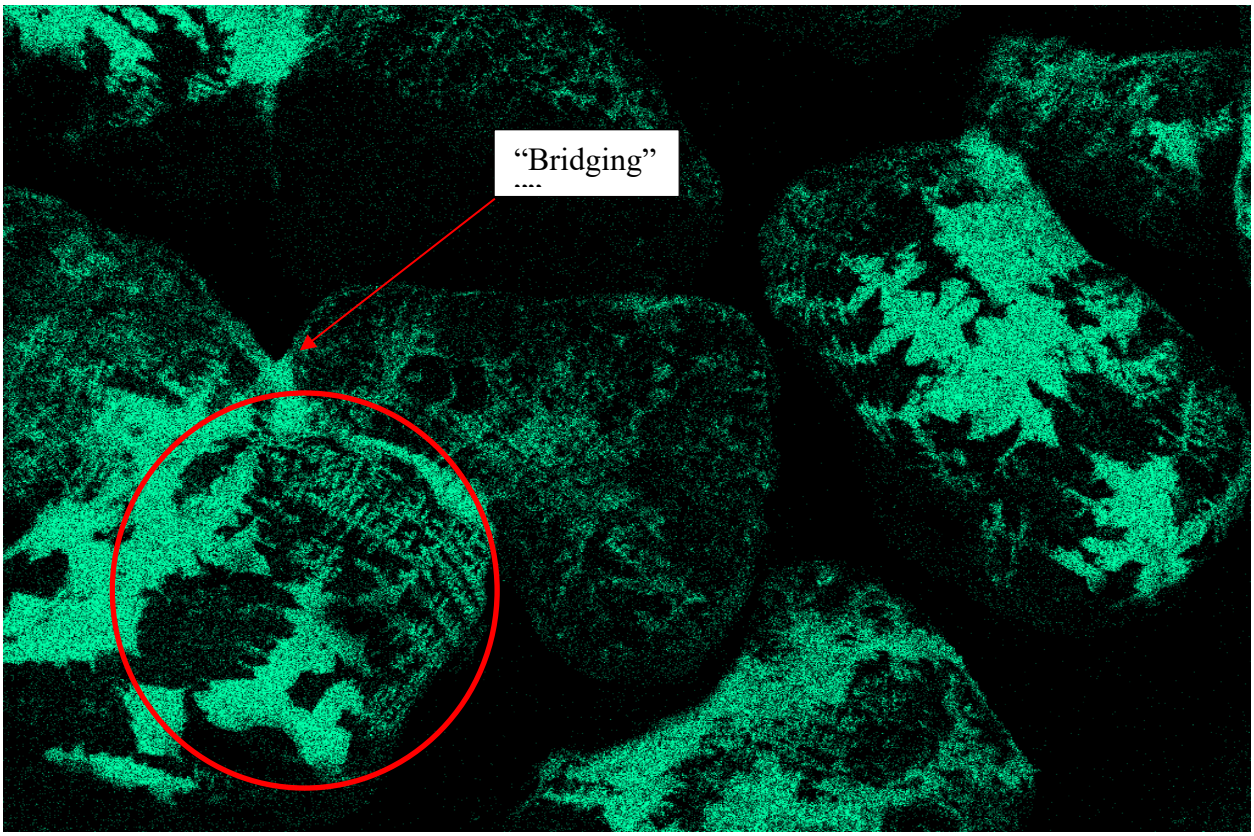

Fig. 3-5: EDS output from T2 - treated Ottawa 50/70 sand, cured at 30°C, corresponding to chlorine (Cl).

3.2 Depth Study

Results from the depth study are presented below in Fig. 3-6 through Fig. 3-7.

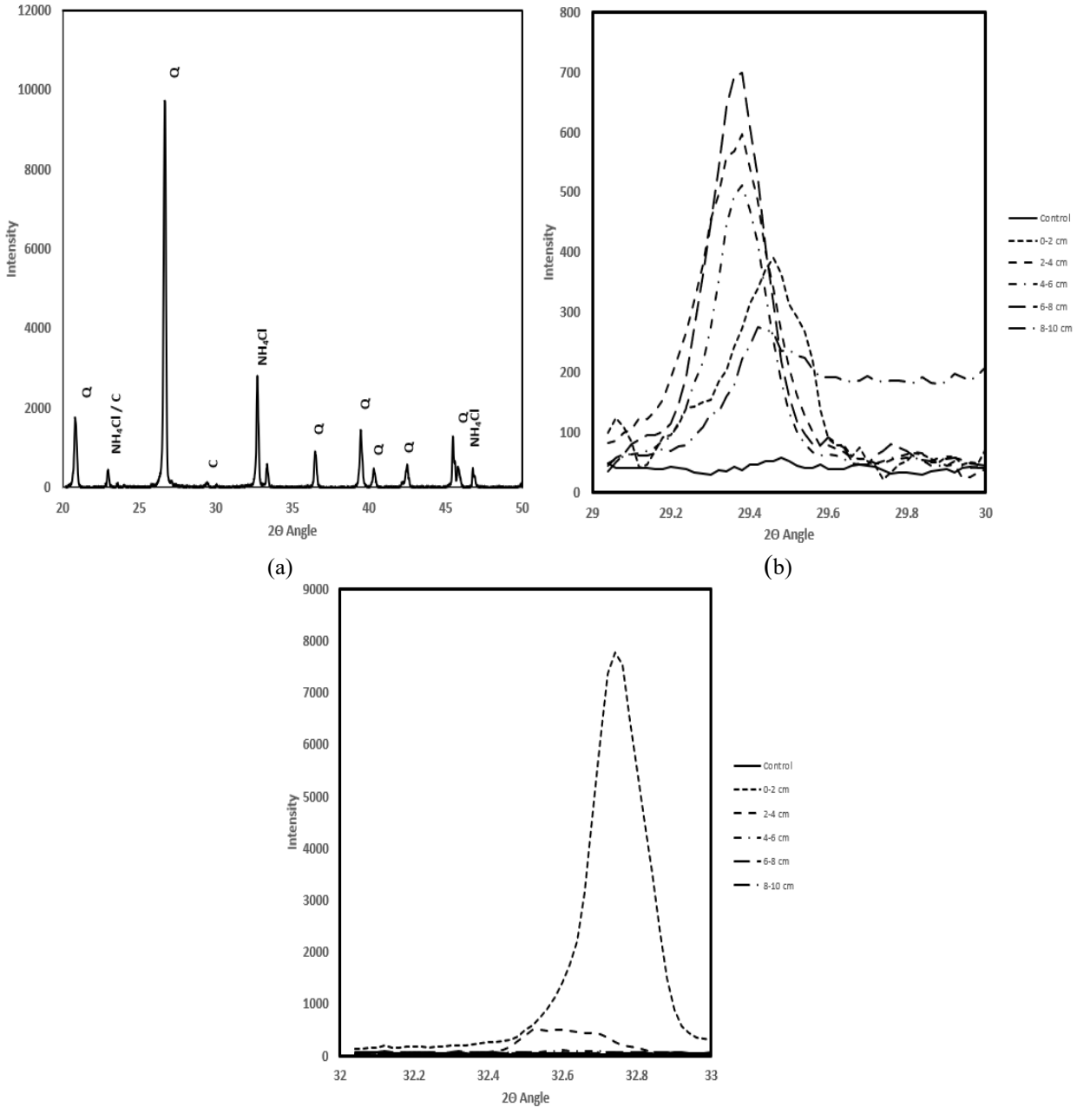

(a) (b)

(c)

Fig. 3-6: Treated Native Beach Sand, cured at 100°C. (a) XRD pattern from D1- the surface of the sample, (b) a peak at 29.40°, corresponding to calcite, plotted at various depths within the sample, (c) a peak centered around 32.64°, corresponding to ammonium chloride and vaterite. Note how these peak decreases as a function of depth.

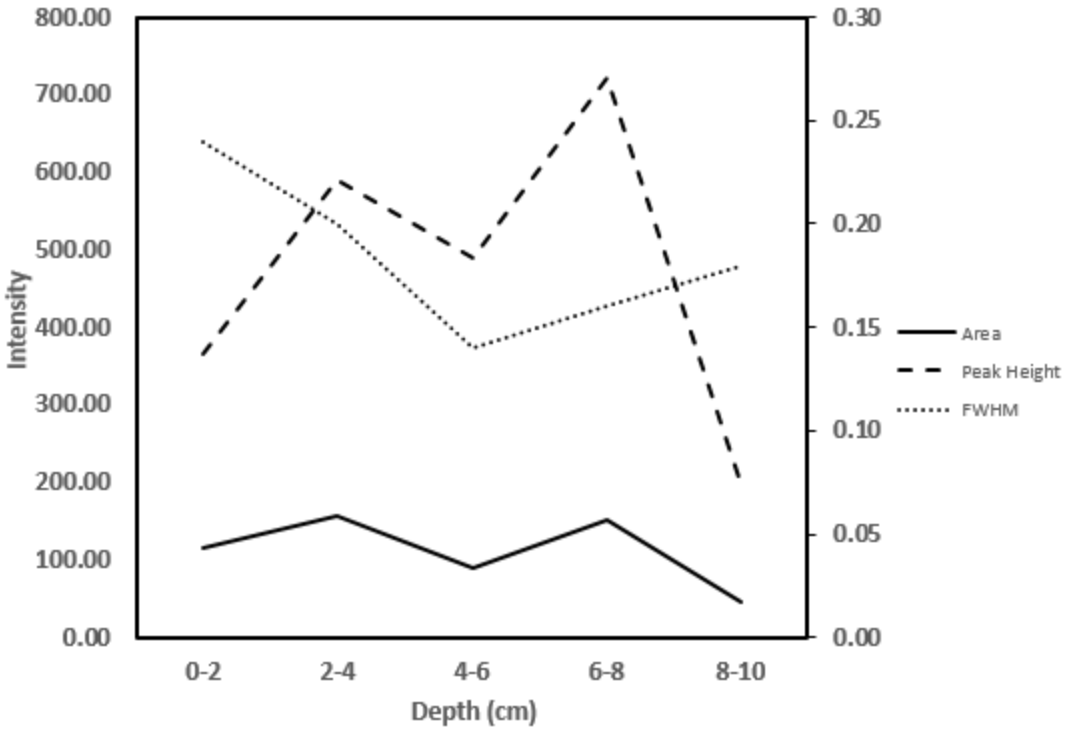

Fig. 3-7: Area, peak height, and FWHM of the prominent $CaCO_3$ peak at 29.40° at various depths in the sample. Area remains consistent, while peak height increases, until both significantly decrease after 8 cm. FWHM has a downward trend.

3.3 Addition of Magnesium

Results from the magnesium study are presented below in Fig. 3-8 through Fig. 3-15.

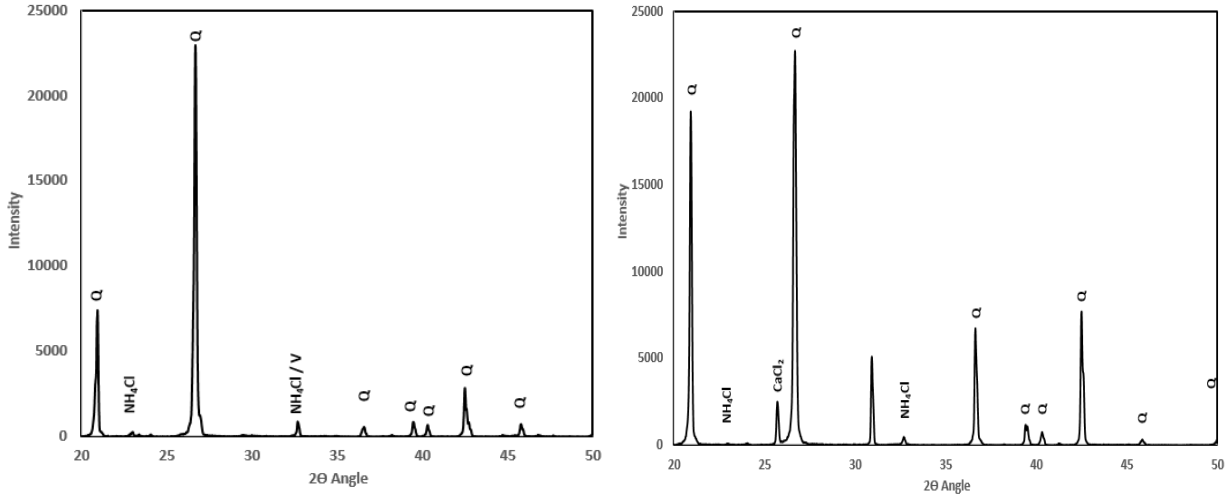

Fig. 3-8: XRD spectrum for Treated Native Beach Sand, cured at 30°C, with varying levels of magnesium chloride added to a 2.5 M Urea/$CaCl_2$ solution. (a) Mg1 - 0.5 M $MgCl_2$ added, and (b) Mg2 - 1.0 M $MgCl_2$ added

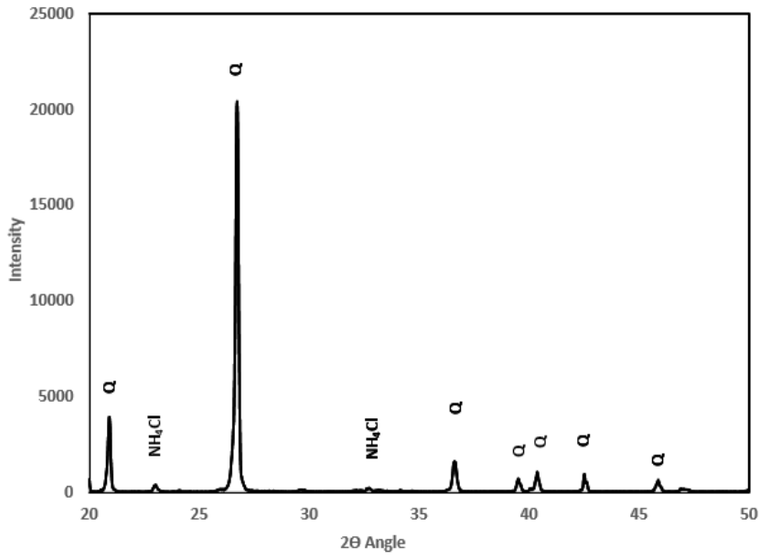

Fig. 3-9: XRD spectrum from Mg3 - Treated Native Beach Sand, cured at 30°C, with 2.5 M $MgCl_2$ added to a 2.5 M Urea/$CaCl_2$ solution

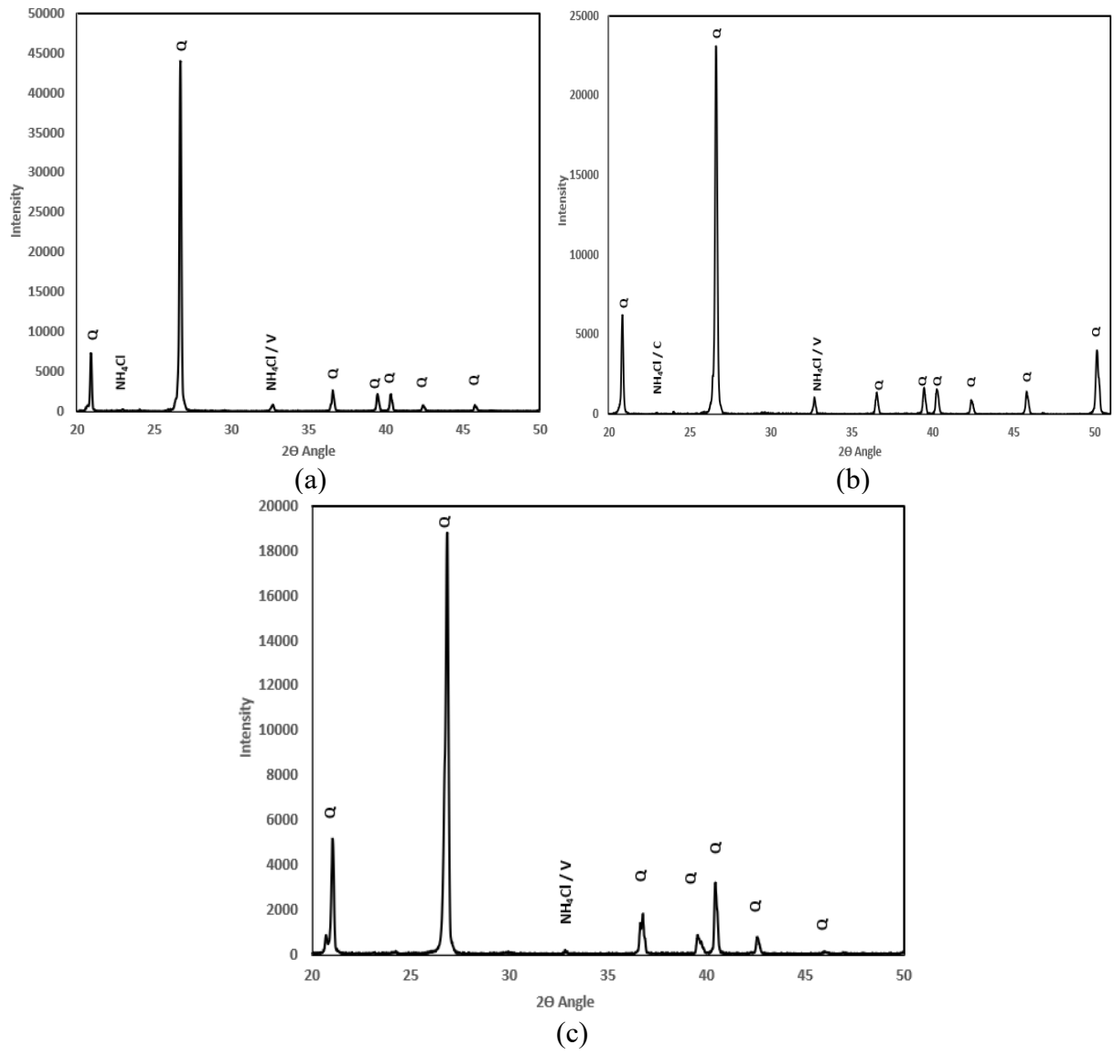

Fig. 3-10: XRD spectrum for Treated Ottawa 50/70 Sand, cured at 30°C, with varying levels of magnesium chloride added to a 2.5 M Urea/$CaCl_2$ solution. (a) Mg4 - 0.5 M $MgCl_2$ added, (b) Mg5 - 1.0 M $MgCl_2$ added, and (c) Mg6 - 2.5 M $MgCl_2$ added.

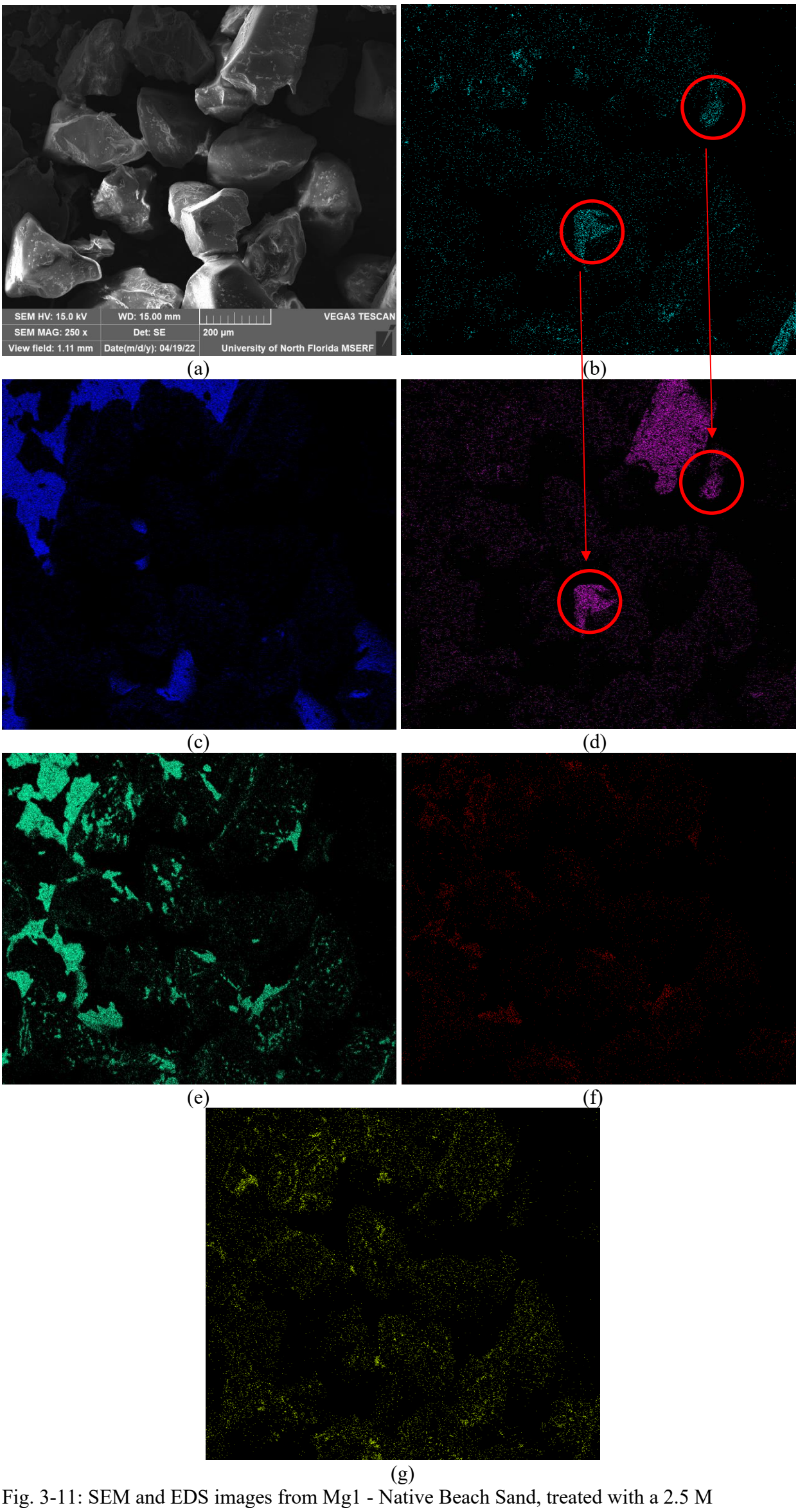

Fig. 3-11: SEM and EDS images from Mg1 - Native Beach Sand, treated with a 2.5 M Urea/$CaCl_2$ and 0.5 M $MgCl_2$ solution, cured at 30°C. (a) SEM image; (b) EDS calcium reading; (c) EDS carbon reading; (d) EDS aluminum reading; (e) EDS chlorine reading; (f) EDS nitrogen reading; and (g) EDS magnesium reading.

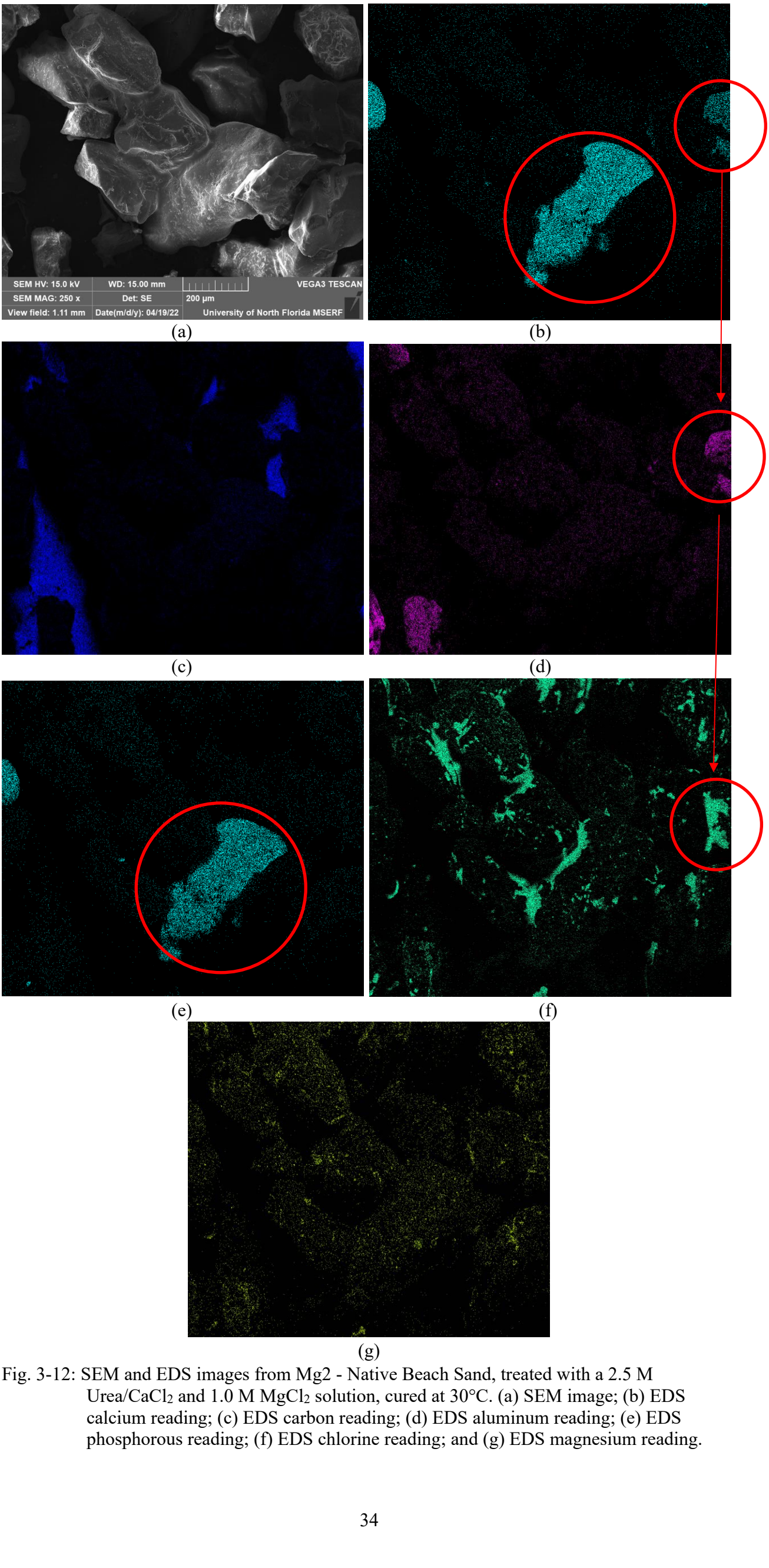

Fig. 3-12: SEM and EDS images from Mg2 - Native Beach Sand, treated with a 2.5 M Urea/$CaCl_2$ and 1.0 M $MgCl_2$ solution, cured at 30°C. (a) SEM image; (b) EDS calcium reading; (c) EDS carbon reading; (d) EDS aluminum reading; (e) EDS phosphorous reading; (f) EDS chlorine reading; and (g) EDS magnesium reading.

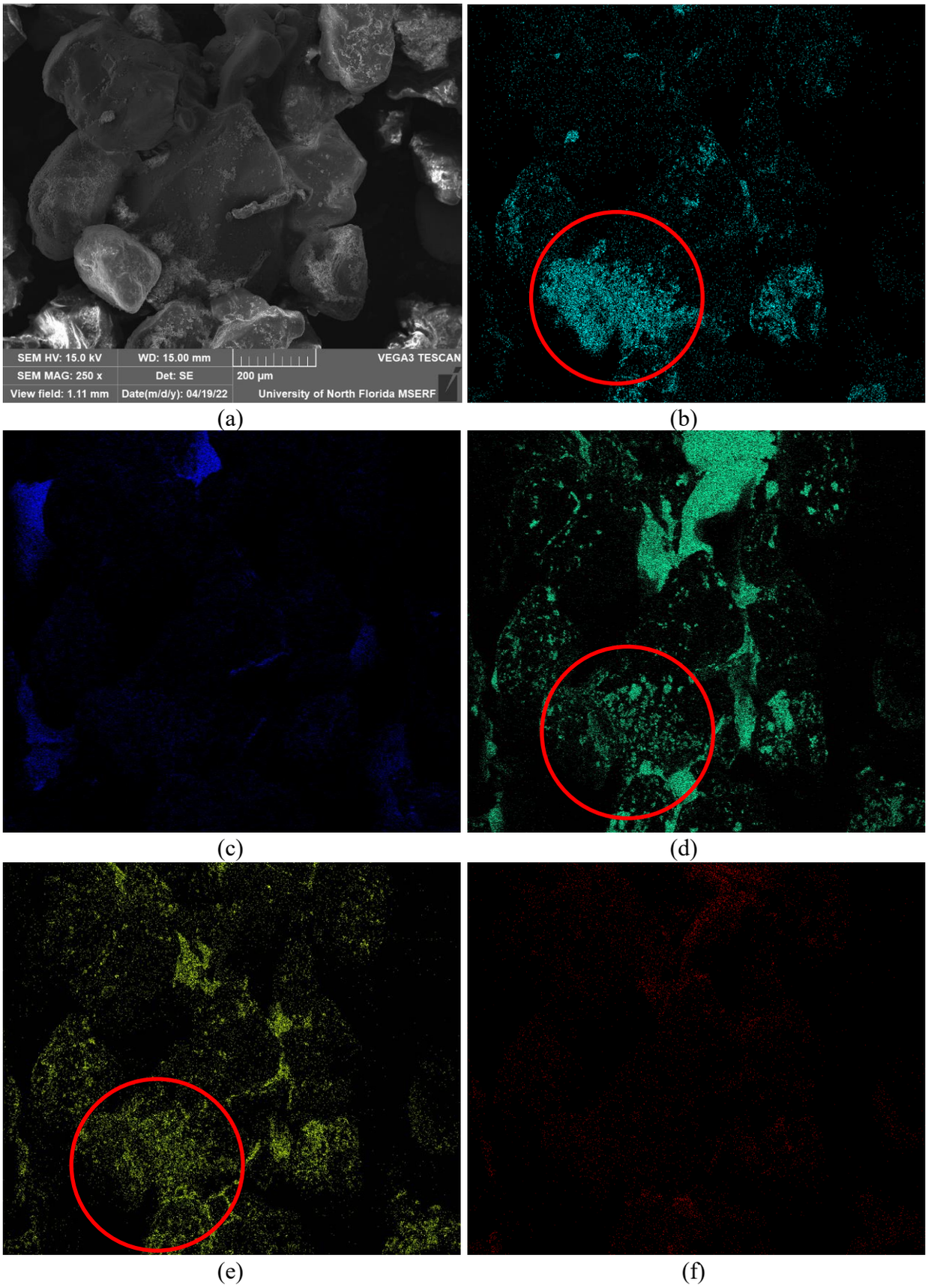

Fig. 3-13: SEM and EDS images Mg3 - Native Beach Sand, treated with a 2.5 M Urea/$CaCl_2$ and 2.5 M $MgCl_2$ solution, cured at 30°C. (a) SEM image; (b) EDS calcium reading; (c) EDS carbon reading; (d) EDS chlorine reading; (e) EDS magnesium reading; and (f) EDS nitrogen reading.

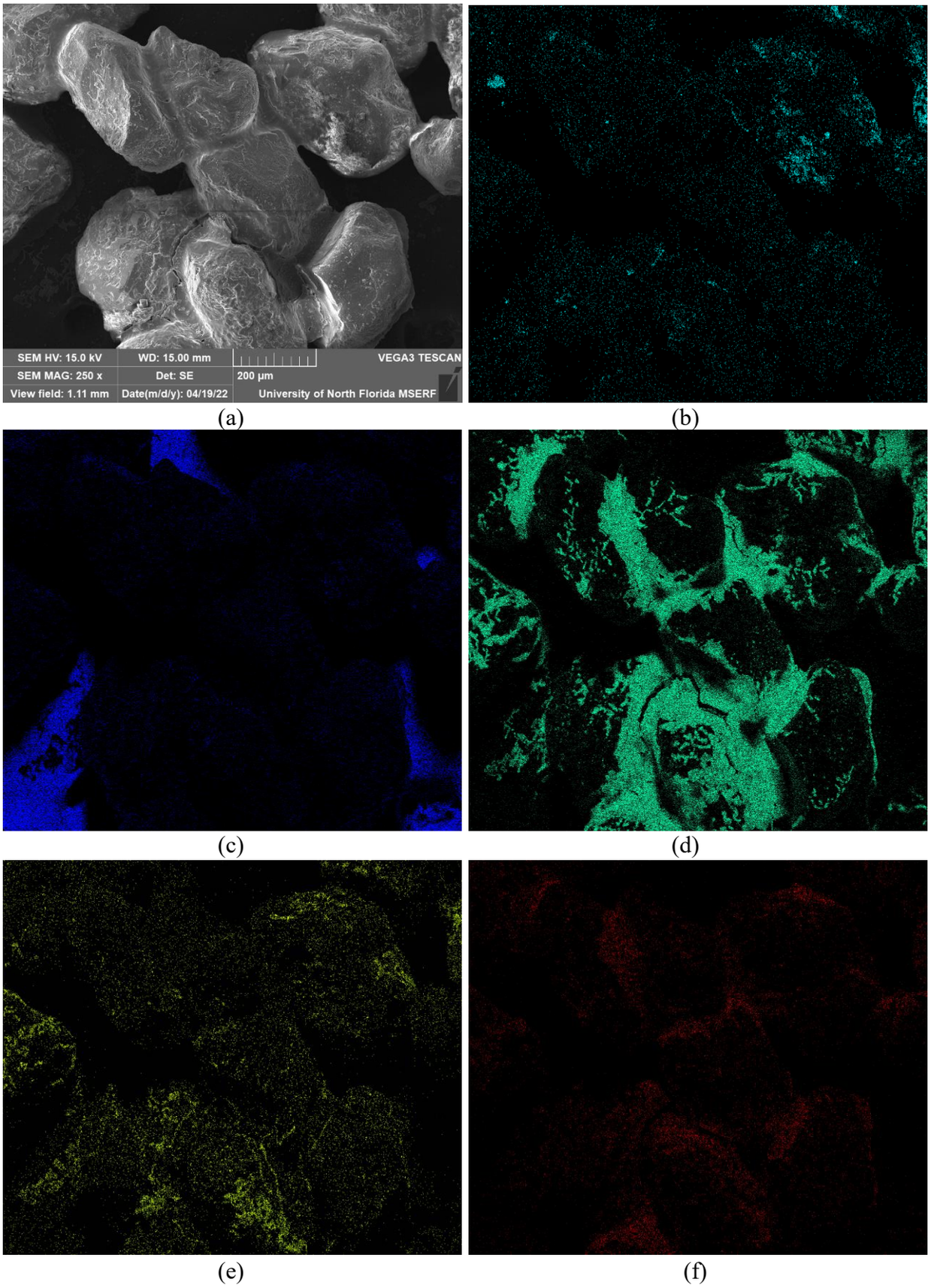

Fig. 3-14: SEM and EDS images from Mg5 - Ottawa 50/70 Sand, treated with a 2.5 M Urea/$CaCl_2$ and 1.0 M $MgCl_2$ solution, cured at 30°C. (a) SEM image; (b) EDS calcium reading; (c) EDS carbon reading; (d) EDS chlorine reading; (e) EDS magnesium reading; and (f) EDS nitrogen reading

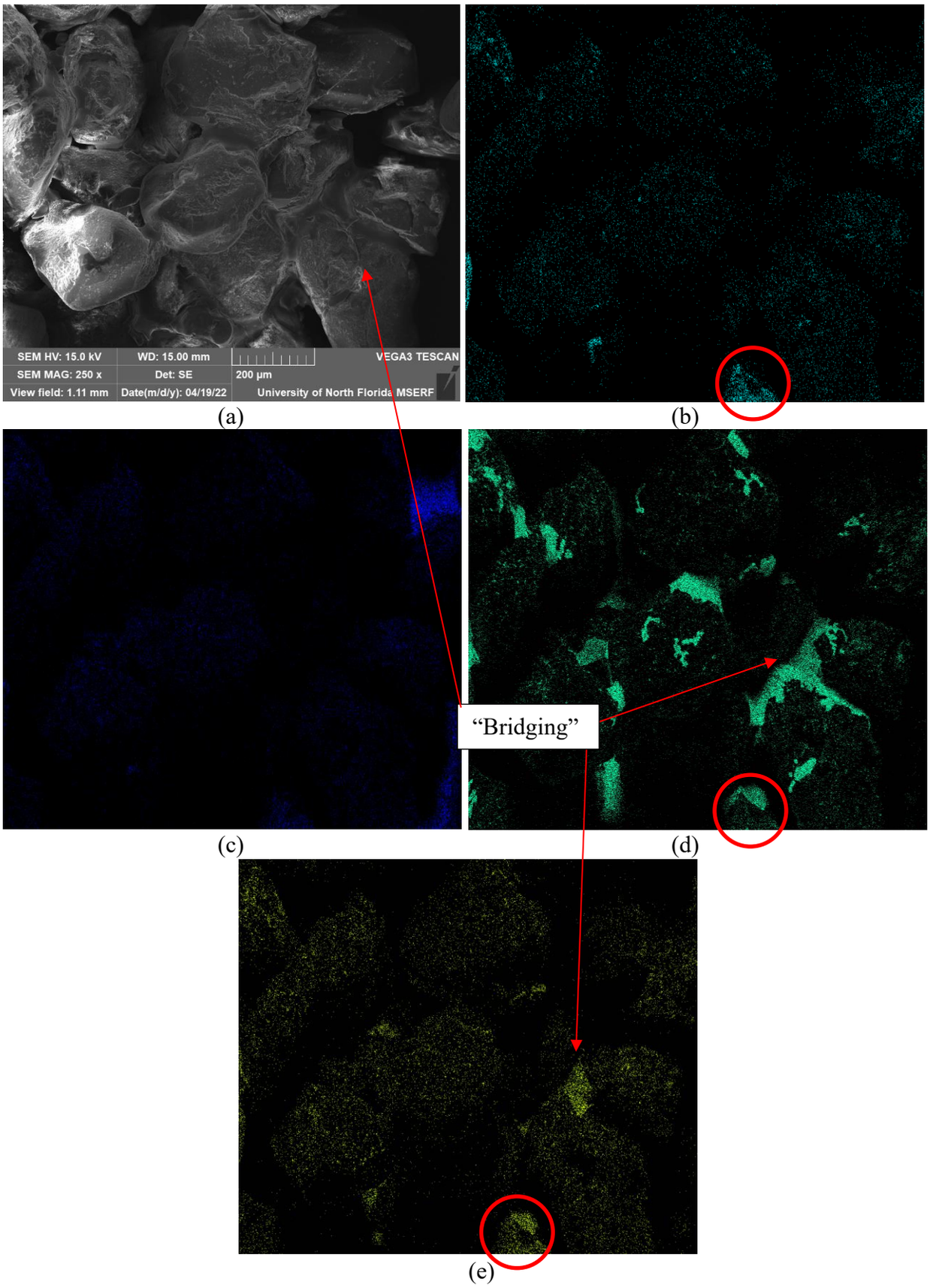

Fig. 3-15: SEM and EDS images from Mg6 - Ottawa 50/70 Sand, treated with a 2.5 M Urea/$CaCl_2$ and 2.5 M $MgCl_2$ solution, cured at 30°C. (a) SEM image; (b) EDS calcium reading; (c) EDS carbon reading; (d) EDS chlorine reading; and (e) EDS magnesium reading.

3.4 X-Ray Diffraction (XRD) and Scanning Electron Microscope (SEM) for Control

Results from the untreated native beach sand and Ottawa 50/70 are presented below in Fig. 3-16 through Fig. 3-19.

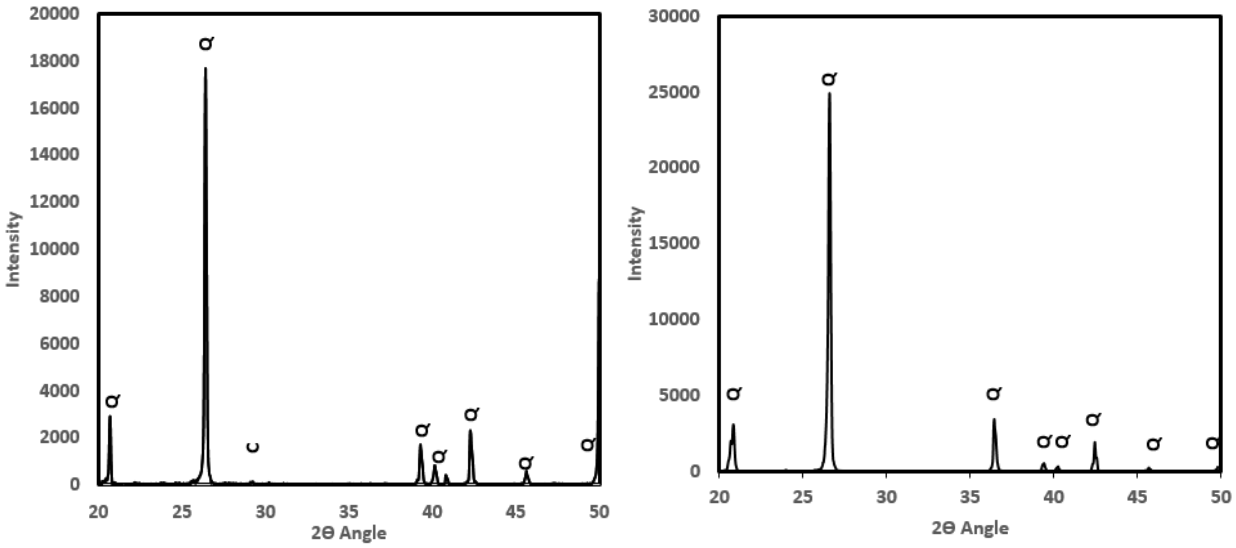

(a) (b)

Fig. 3-16: XRD Patterns for untreated sand samples; (a) Untreated native beach sand, with a prominent quartz diffraction pattern, and small calcite signal; (b) untreated Ottawa 50/70 sand, with a prominent quartz diffraction pattern.

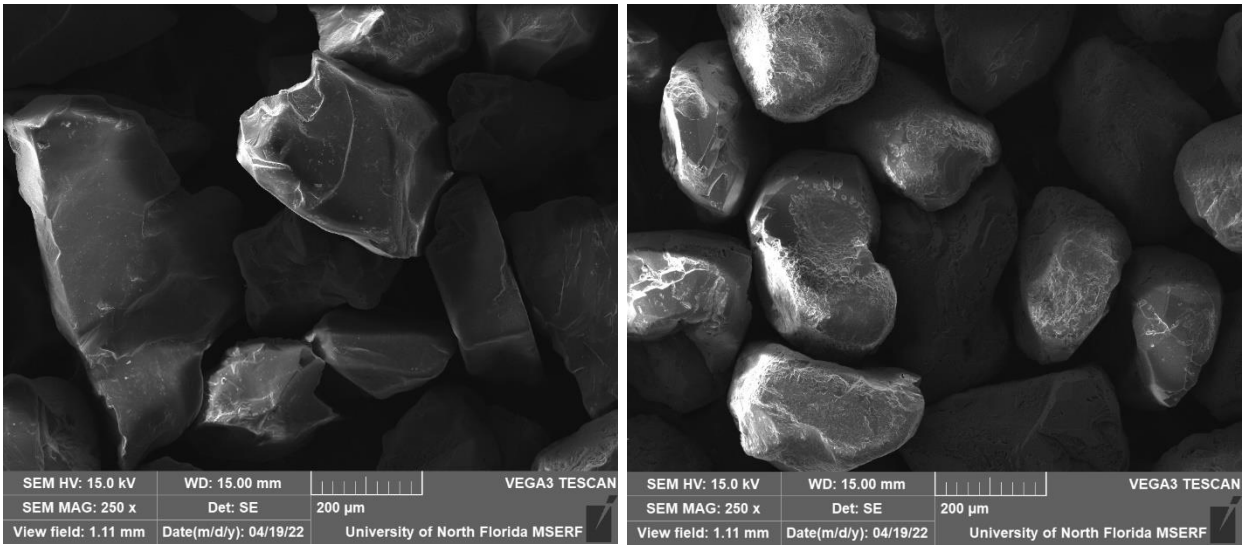

(a) (b)

Fig. 3-17: SEM images for the untreated sand samples. (a) shows untreated native beach sand; (b) shows untreated Ottawa 50/70 sand.

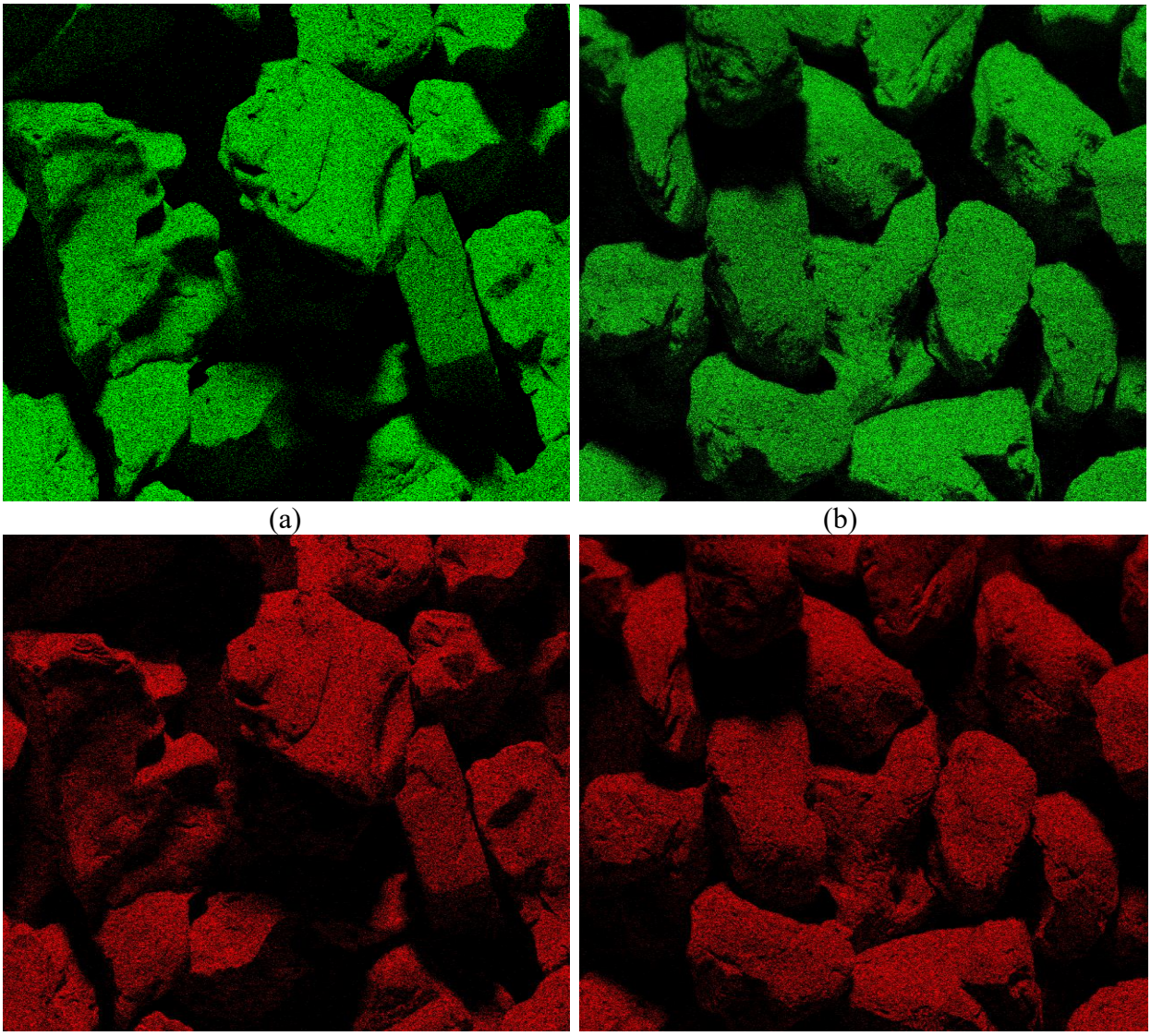

(a) (b)

(c) (d)

Fig. 3-18: EDS images for untreated sand samples. (a) shows the presence of silicon in green for untreated native beach sand; (b) shows the presence of silicon in green for untreated Ottawa 50/70 sand; (c) shows the presence of oxygen in red for untreated native beach sand; (d) shows the presence of oxygen in untreated Ottawa 50/70 sand.

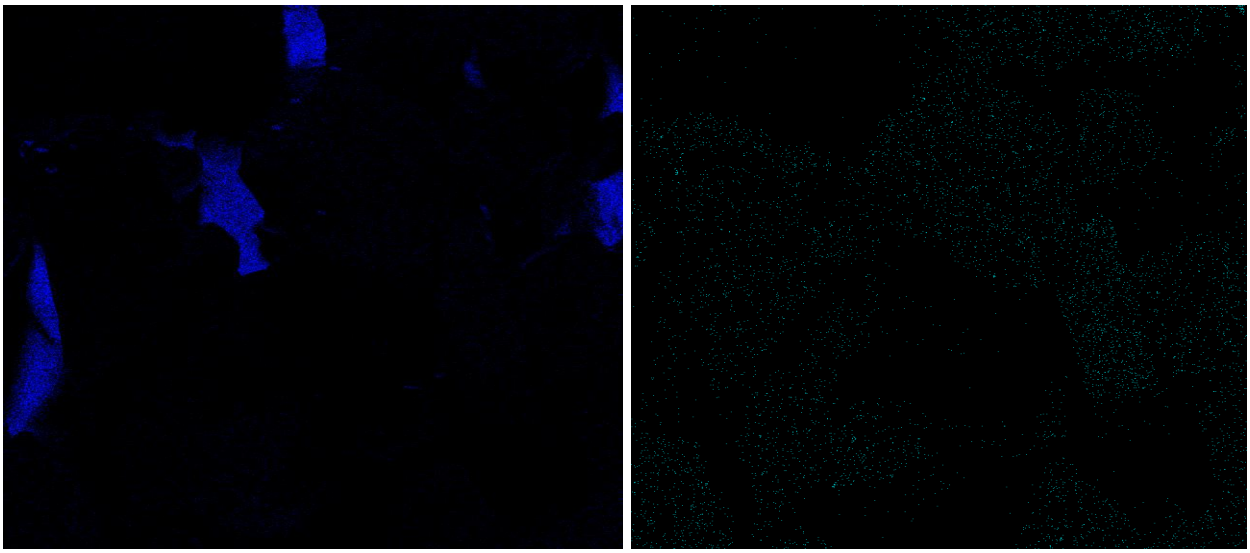

(a) (b)

Fig. 3-19: EDS images for untreated native beach sand. (a) shows carbon in blue, the high concentrations of carbon in this image are the conductive carbon tape used to mount samples to the SEM stubs; (b) shows the presence of calcium.

CHAPTER 4
DISCUSSION

4.1 Temperature Study

Fig. 3.1 (a) and (b) show diffraction patterns for treated native beach sand and Ottawa 50/70 sand, cured at 50°C. A quartz diffraction pattern is evident, and the spectrum also shows smaller peaks corresponding to calcite and ammonium chloride. Quartz's most prominent peak is at 26.62° while smaller peaks from quartz are known to occur at Bragg angles of 20.83º, 36.50º, 39.45º, 40.25º, 42.39º, 45.74º, and 50.1º. When analyzing peaks for relative $CaCO_3$ phase fractions, one of the difficulties is that the quartz spectrum masks many of the prominent peaks for aragonite, calcite, and vaterite. Another difficulty is that the intensity for the peaks not masked by quartz, such as the most prominent peak for calcite at 29.40°, is typically lowFr. As such, the less intense peaks in the calcite spectrum are often difficult to distinquish from noise. One solution is to look for substrates that have diffraction patterns that are not as closely matched as quartz and $CaCO_3$. Peaks for calcite and ammonium chloride are seen at 29.40° and 32.65°, respectively. Both calcite and ammonium chloride have a peak at approximately 23°, which can be seen in Fig. 3.1 (a) and (b).

Fig. 3-2 (a) and (b) show the area, peak height, and FWHM of the $CaCO_3$ peaks at temperatures ranging from 20°C to 50°. As shown in Fig. 3-2(a), for treated Native Beach Sand, as temperature increased, area of the calcite peak increased, peak intensity increased, and FWHM increased. Taken together, these results indicate that as temperature increased, the quantity of precipitated $CaCO_3$ also increased. An increase in FWHM means at higher temperatures, smaller crystallite sizes are being produced, and could be indicative of faster than desired reaction kinetics because heat drives off water.

Fig. 3-2(b) shows the treated Ottawa 50/70 data. Unlike the treated native beach sand, the area under the $CaCO_3$ curves at 20°C and 50°C remained relatively consistent. However, there was an increase in area at 30°C, and the peak height increased at 30°C. These results imply then that there may be some optimal cure temperature that maximizes $CaCO_3$ precipitation in Ottawa 50/70 sand somewhere near 30°C, or, that this data point was an outlier. The trend of $CaCO_3$ precipitation with increased temperature should be to increase. Further testing is recommended.

As shown in Fig. 3-2(a) and (b), there was a dominant peak observed at 32.65°, which reflects the presence of ammonium chloride. As temperature increased, the area under the curve associated with this peak, and the height associated with this peak also increased. This could indicate that as the temperature increases and dehydration of the sample increases, more salts are precipitating. It remains unclear how these results affect specimen erodibility. During future work, more physical testing will be conducted to analyze how (or if) this precipitated salt affects erodibility.

As shown in Fig. 3-3, calcium, carbon, chlorine, and oxygen were present in the treated native beach sand. There is a substantial portion of the sand that does not have a chlorine signal, yet strong overlap of the calcium, carbon, and oxygen signals. This is indicative of $CaCO_3$ precipitated via the MICP process. SEM data (Fig. 3-3(a)) indicate that calcium carbonate appears to be forming like a coating in the bottom lefthand corner of the image. Overall, the SEM and EDS images appear to confirm XRD data in the sense that taken together, they appear to indicate that calcium carbonate was precipitated. If synthetic calcite and aragonite precipitate from solution one would expect to see well defined faceted microscopic crystals with either rhombic or acicular/needle-like morphology. If, however, these crystals are resulting from the MICP process, then one would expect to see a more globular patchwork of submicron crystals that have surface

morphology/texture that could be remnant of association with the organic molecules from the bacteria biofilm under which they are formed. If the MICP process is resulting in crystals like that (which would be a thin layer on the surface of the substrate particles) then the diffracted intensity of the MICP phases would be much smaller than expected from the synthetic forms represented in the ICDD.

Fig. 3-4 shows similar results to Fig. 3-3, but with an interesting view of the space between sand grains in the sense that the SEM image appears to show bridging between sand grains. EDS data in Fig. 3-4 and Fig. 3-5 appear to indicate that this bridging may be caused by salt – specifically reprecipitated calcium chloride. Again, it is unclear how these salts will affect erodibility in desaturated specimens like the ones produced here.

4.2 Depth Study

Fig. 3-6 (a) shows a diffraction pattern for treated beach sand. A pronounced quartz spectrum is evident in the XRD spectrum and may mask a weaker $CaCO_3$ signal. Note that a calcite peak attributed to the 104 diffraction plane was observed at a Bragg angle of 29.4°. Another calcite peak should have been observed at a Bragg angle of 23.02°, but the NH_4Cl peak at 22.96° appears to be masking this signal. This could occur if the phases of $CaCO_3$ present do not strongly diffract. Finally, note that once again, significant ammonium chloride appears to have been precipitated as shown by the peaks at angles of 32.65° and 22.96°.

Fig. 3-6 (b) shows a prominent peak at the 29.40° diffraction angle. This peak at this diffracted angle was chosen for analysis because it is the most prominent peak in the calcite spectrum, and it occurs at a unique angle that is not shared with aragonite, vaterite, or quartz. The resulting area under this curve was consistent as a function of depth while the peak intensity associated increased as a function of depth. Higher peak intensities at depth suggest that more calcite was precipitated at depth than at the surface. The data also suggest that significant calcite

may be produced to a depth of approximatley 10 cm. It is unclear how or if this affects erodibility, and further study will be required to investigate this. Further investigation should also be conducted to explore percolation when the treatment solution volume is greater than the volume of the voids for the substrate.

Fig 3-6 (c) shows a prominent peak at a diffraction angle of 32.64° associated with ammonium chloride. Peak intensity as a function of depth in this figure shows that most ammonium choride was precipitated near the surface of the specimen. This could be caused by varying rates of dehydration in the sense that portions of the specimen near the surface dehydrate faster than portions of the sample at depth. The implications associated with this for erodibility remain unclear, but it is interesting to note that the precipitated ammonium chloride did appear to inhibit calcite precipitation. Calcite precipitation was highest in regions of the specimen where ammonium chloride precipitation was lowest, based on peak intensities from the depth study.

As seen in Fig. 3-7, as depth increased, the area remained consistent while peak intensity of calcite increased. For the area to remain consistent, while peak intensity increases, the FWHM must decrease. This is confirmed via outputs from Fityk 1.3.1. and is seen in Fig. 3-14. At the surface, the FWHM is 0.24, and decreases to a minimum of 0.14. This suggests that the $CaCO_3$ crystallites being formed are bigger, relatively, than crystallites being formed at the surface of the sample. This is indicative of varying reaction kinetics. When the growth rate of crystals is slowed, they can grow larger with fewer imperfections.

4.3 Addition of Magnesium

Fig. 3-8 through Fig. 3-10 show XRD spectra for treated native beach sand and Ottawa 50/70 sand. In the initial indexing of the diffraction patterns from Mg1 through Mg6, it appeared that calcium carbonate was not produced. Any peaks corresponding to calcium carbonate, such as calcite, at 29.40°, were very small, and were not distinguishable from background noise.

Precipitation of salts was evident in every XRD spectra. To investigate further, SEM and EDS images were taken for every sample.

As seen in Fig. 3-11 (b), there is a strong calcium signal, but as shown in Fig. 3-11 (c), this signal does not appear to coincide with the signal from carbon. The strong carbon signals are from the conductive carbon tape used with the aluminum SEM stubs. There is a good overlap between the calcium signal and the aluminum signal shown in Fig. 3-11 which could indicate calcium aluminate was formed. Fig. 3-11 (e) shows a large presence of chloride, which appears to coindcide with nitrogen shown in Fig. 3-11 (f) and magnesium shown in Fig. 3-10 (g), This indicates that salts (particularly magnesium chloride) may have precipitated, but the presence of calcium carbonate, if present, is small.

Results in Fig. 3-12 are similar in the sense that they imply that $CaCO_3$ preciptiation was likely small. As seen in Fig. 3-12 (b), there is strong concentration of calcium, but it does not have a significant overlap with carbon shown in Fig. 3-12 (c). On the contrary, the calcium appears to overlap with aluminum shown in Fig. 3-12 (d) ,phosphorus shown in Fig. 3-12 (e) and chlorine shown in Fig. 3-12(f). This indicates that there may be bone fragments the specimen. Chloride shown in Fig. 3-12 (f) and magnesium shown in Fig. 3-12 (g) appear to overlap to some extent. Overall, it appears that calcium carbonate was not produced from this chemical reaction.

Fig. 3-13 shows that like the other two native beach sand outputs, there is a strong calcium concentration in the bottom left of Fig. 3-13 (b) but observed carbon in that region of Fig. 3-13 (c) was minimal. The calcium appears to overlap well with both magnesium (Fig. 3-13 (d)) and chlorine (Fig. 3-13 (e)), indicating that $MgCl_2$, and $CaCl_2$, likely reprecipitated. There is a small overlap between Fig. 3-13 (e) and Fig. 3-13 (f), which could indicate the presence of ammonium chloride.

Overall, these data appear to indicate that minimal calcification occurred. However, because NH_4Cl was produced, the data imply that urealysis must have occurred. Note from Eq. 1-4 that ammonium only occurs after carbamic acid hydrolysis. As such, these results imply that the pH associated with the reaction was not raised sufficiently to jumpstart the shift in bicarbonate equilibrium. This implies that the presence of high-concentration Mg^{2+} like the solutions tested in this study may inhibit increases in pH – perhaps through formation of $Mg(OH)_2$. This result requires further investigation.

Fig. 3-14, shows a small concentration of calcium in the top left corner of (b). There does not seem to be any overlap between Fig. 3-14 (b) and Fig. 3-14 (c), which indicates that calcium carbonate is not present in this sample. There is a significant concentration of chlorine, which can be seen in Fig. 3-14 (d). The chlorine reading has significant overlap with the calcium, magnesium, and nitrogen readings, as can been seen in Fig. 3-14 (b), (e), and (f). These data shows that calcium carbonate was likely not produced. Instead, these data suggest that the byproduct of this treatment was mostly reprecipitated salt.

Fig. 3-15 (b), near the bottom, shows the strongest concentration of calcium. This calcium overlaps well with Fig. 3-15 (d) and (e), indicating the presence of calcium chloride and magnesium chloride. The carbon concentrations are more pronounced then the other two Ottawa 50/70 experiments, as seen in Fig. 3-15 (c), but there is no significant overlap with calcium. Fig. 3-15 (e) and (d) show a salt bridge between two sand grains, this indicates a $MgCl_2$ bridge.

Further investigation is needed for this study. Compared to Fig. 3-3 and Fig. 3-4, the calcium/carbon overlap is significantly lower. Both images were taken from treated sand samples, cured at 30°C, the only difference being the added magnesium. It is worth noting that during the magnesium study, the curing oven may have malfunctioned. It is not known whether or not the

samples reached 30°C, and if they did, how long they cured for at 30°C. Thus, investigators were unable to interpret the experimental data as intended. Investigators suggest further investigation into this study.

4.4 Control Testing

As shown in Fig. 3-16 (a) and (b), the dominant diffraction angle for untreated specimens was 26.62° for Native Beach sand and Ottawa 50/70. This angle corresponds to quartz. Smaller diffraction intensities for quartz were observed at Bragg angles of 20.83°, 36.50°, 39.45°, 40.25°, 42.39°, 45.74°, and 50.1°. In addition, a small peak diffraction at an angle of 29.4° was observed in the native beach sand. This peak corresponds to calcium carbonate – particularly calcite. Peaks with smaller relative intensities are difficult to see in the diffraction pattern because they are (a) masked by the more prominent quartz peaks, or (b) indistinguishable from background noise. These results are expected because Ottawa 50/70 and beach sand are primarily quartz. The presence of calcite in beach sand is also expected and is likely the result of coral and/or seashells.

Fig. 3-17 shows SEM images for (a) native beach sand and (b) Ottawa 50/70 sand. Fig. 3-18 show (EDS) outputs for untreated Native Beach Sand and Ottawa 50/70 Sand. Fig. 3-18 (a) and (b) show EDS outputs for silicon in both native beach sand and Ottawa 50/70 sand, respectively. Fig. 3-18 (c) and (d) show EDS outputs for oxygen in both native beach sand and Ottawa 50/70 sand, respectively. The mineral corresponding to the main XRD diffraction angles and peak intensities is quartz, whose chemical formula is SiO_2. The EDS readings for Silicon (Si) and Oxygen (O) for the Native Beach Sand and Ottawa 50/70 sand show significant overlap, and with the indexed diffraction pattern, confirm the presence of SiO_2, quartz.

Fig. 3-19 (a) and (b) show the presence of Carbon and Calcium in the Native Beach Sand, which could indicate Calcium Carbonate, $CaCO_3$. The areas with a significant concentration of carbon come from the conductive carbon tape used during sample preparation, but there is some

overlap between the carbon and calcium maps, which is an expected output from beach sand due to the presence of seashells and coral. Calcium was not present in the Ottawa 50/70 EDS outputs.

CHAPTER 5
SUMMARY AND CONCLUSIONS

To summarize, investigators hoped to determine (1) how $CaCO_3$ production varies as a function of post-treatment temperature when sand was treated via MICP and a surface percolation treatment technique; (2) how $CaCO_3$ production varies as a function of depth when treated via MICP and a surface percolation treatment technique; and (3) how the $CaCO_3$ phases change as a function of concentration of added Mg^{2+}. Investigators hypothesized that (1) increasing temperature would increase $CaCO_3$ formation; (2) $CaCO_3$ formation would decrease with depth; and (3) that the increased concentration of Mg^{2+} would promote aragonite growth and inhibit calcite growth. Several series of experiments were conducted to test these hypotheses. Results showed the following:

4. Increase in temperature led to an increase in peak height, and area under the prominent calcite peak for native beach sand. In Ottawa 50/70 sand, the max peak height and area was achieved at a temperature of 30°C. More investigation needs to be completed. The data at 50°C could be an outlier.

5. The amount of CaCO3 produced varied as a function of treatment percolation. Peak height increased and area was consistent under the prominent calcite peak until 8 cm in depth, where both peak height and area significantly decreased. Results were the opposite of the initial hypothesis. This could be a result of faster dehyradtion rates at the surface, causing more salts to precipitate. More investigations should be conducted on how soil moisture affects $CaCO_3$ formation.

6. Further investigation is needed to determine the affect Mg^{2+} has on promoting aragonite growth and inhibiting calcite growth.

In addition, further investigation needs to be conducted to fully determine how $CaCO_3$ production varies as a function of temperature, depth, and the addition of Mg^{2+}. Investigators suggest more testing, with multiple specimens prepared and tested the same way, to gain a more quantitative understanding of the process. Finding a substrate with a more dissimilar diffraction pattern to $CaCO_3$ would help distinguish smaller $CaCO_3$ peaks and convolute curves. Using a smaller step size and slower scan speed on the XRD would help get a better resolution. This would

decrease noise, and increase clarity, making it easier to convolute curves and get more accurate data. Lastly, erosion testing should be done simultaneously to empirically quantify the benefits of $CaCO_3$ and salt precipitation. Testing needs to be conducted that varies soil moisture content and pH, to gain a better understanding of how those two parameters affect $CaCO_3$ precipiation and morphology.

Complementary characterization techniques provided clues on the MICP particle phases and morphologies in the context of treated specimen erodibility in the sense that results show how calcification varies as a function of depth, and calcification is inversely related to erodibility. However, erosion testing data vis-à-vis these atomic data are needed in future work to determine exactly how these results translate toward practical field applications. Multiple forms of characterization can be done including physical (erosion testing), chemical (acid wash), spectroscopy (diffraction), and morphological (imaging) can be used together to better understand the MICP process.

LIST OF REFERENCES

Achal, V., Peng, J., and Z., L. (2019). "Influence of temperature on microbially induced calcium carbonate precipitation for soil treatment". *PLoS One*, 14(6), e0218396. https://doi.org/10.1371/journal.pone.0218396

ATSM. (2014). "Standard Test Methods for Specific Gravity of Soil Solids by Water Pycnometer". West Conshohocken, PA: ASTM International.

Oxford. Aztec [Computer Software]. (2021). 5.1.7829.

Briaud, J. L., Bernhardt, M., and Leclair, M. (2011). "The Pocket Erodometer Test: Development and Preliminary Results". *Geotechnical Testing Journal*, 35(2), 342-352.

Briaud, J. L., Ting, F.C.K, Chen, H.C., Cao, Y. (2001). "Erosion Function Apparatus for Scour Rate Predictions". *Journal of Geotechnical and Geoenvironmental Engineering*, 127:2(105), 105-113.

Chandra, A., and Ravi, K. (2020). "Effect of Magnesium Incorporation in Enzyme-Induced Carbonate Precipitation (EICP) to Improve Shear Strength of Soil". *Advances in Computer Methods and Geomechanics*, 333-346.

Chek, A., Crowley, R., Ellis, T. N., Durnin, M., and Wingender, B. (2021). "Evaluation of Factors Affecting Erodibility Improvement for MICP-Treated Beach Sand". *Geotechnical and Geoenvironmental Engineering*.

Choi, S.-G., Park, S.-S., Wu, S., and Chu, J. (2014). "Methods for Calcium Carbonate Content Measurement of Biocemented Soils". *Journal of Materials in Civil Engineering*, 29 (11): 06017015.

Dejong, J. T., Fritzges, M.B., Nusslein, K. (2006). "Microbially Induced Cementation to Control Sand Response to Undrained Shear". *Journal of Geotechnical and Geoenvironmental Engineering*, 132(11).

Dejong, J. T., Mortensen, B. M., Martinez, B. C., and Nelson, D. C. (2010). "Bio-mediated soil improvement". *Ecological Engineering*, 197-210.

Do, J., Montoya, B. M., and Gabr, M. A. (2020). "Scour Mitigation and Erodibility Improvement Using Microbially Induced Carbonate Precipitation". *Geotechnical Testing Journal*.

Ebnesajjad, S. (2011). 4 - Surface and Material Characterization Techniques. In *Handbook of Adhesives and Surface Preparation* (pp. 31-48). William Andrew Publishing.

Hargis, C. W., Chen, I. A., Devenney, M., Fernandez, M. J., Gilliam, R. J., and Thatcher, R. P. (2021). "Calcium Carbonate Cement: A Carbon Capture, Utilization, and Storage (CCUS) Technique". *Materials*, 2079.

Heriansyah, P., Hideaki, Y., Naoki, K., Debendra, N., and Chih-Wei, L. (2016). "Effect of Magnesium as Substitute Material in Enzyme-Mediated Calcite Precipitation for Soil-Improvement Technique". *Frontiers in Bioengineering and Biotechnology*.

International Centre for Diffraction Data (2021). Powder Diffraction File - 4+. [Computer Software]

Jian, Z., and Hejing, W. (2003). "The Physical Meanings of 5 Basic Parameters for an X-Ray Diffraction Peak and Their Application". *Chinese Journal of Geochemistry*, 38-44.

Krajewska, B. (2018). "Urease-aided calcium carbonate mineralization for engineering applications: a review". *Journal of Advanced Research*, 59-67.

Liu, K. J. (2021). "An experimental study of mitigating coastal sand dune erosion by microbial- and enzymatic-induced carbonate precipitation". *Acta Geotech*, 467-480.

Microsoft Corporation. (2016). "Microsoft Excel". Retrieved from https://office.microsoft.com/excel.

Mehta, A. (1991). "Review Notes on cohesive sediment erosion". *Proc. Coastal Sediments* (pp. 40-43). Reston, VA: ASCE.

Morse, J. W., Arvidson, R. S., and Luttge, A. (2007). "Calcium Carbonate Formation and Dissolution". *Chemical Reviews*, 342-381.

NOAA .(2022). "Local Cimatological Data". National Centers for Environmental Information. https://www.ncdc.noaa.gov/cdo-web/datasets/LCD/stations/WBAN:03853/detail.

Office of Resilience and Coastal Protection. (2021). "Critically Eroded Beaches in Florida". Florida Department of Environmental Protection.

Salifu, E., MacLachlan, E., Iyer, K. R., Knapp, C. W., and Tarantino, A. (2016). "Application of microbially induced calcite precipitation in erosion mitigation and stabilisation of sandy foreshore slopes: a preliminary investigation". *Engineering Geology*, 96-105.

Saracho, A. C., Haigh, S., and Jorat, M. E. (2021). "Flume study on the effects of microbial induced calcium carbonate precipitation (MICP) on the erosional behavior of fine sand". *Géotechnique*, 1135-1149.

Uddin, M. J. (2020). "Synthesis and Characterization of Carbon Sequestering Calcium Carbonate Cement". Jacksonville: University of North Florida.

Wang, Z., Zhang, N., Yong Jin, Q. L., and Xu, J. (2020). "Application of microbially induced calcium carbonate precipitation (MICP) in sand embankments for scouring/erosion control". *Marine Geosources & Geotechnology*, 1459-1471.

Wojdyr, M. (2010). "Fityk: a general-purpose peak fitting program". *Journal of Applied Crystallography*, 4 3, 1126-1128.

Xu, X., Guo, H., Cheng, X., and Li, M. (2020). "The promotion of magnesium ions on aragonite precipitation in MICP process". *Construction and Building Materials*.

Zhang, Y., Guo, H., and Cheng, H. (2015). "Role of Calcium sources in the strength and microstructure of microbial mortar". *Construction and Building Materials*, 160-167.

BIOGRAPHICAL SKETCH

Justin Mulloney was born and raised in Cincinnati, Ohio and a 2016 graduate of the University of Cincinnati. He earned a Bachelor of Science in Aerospace Engineering. Justin Mulloney was commissioned as a Naval Officer on January 27, 2017. Since commissioning, Justin has served as a Construction Manager at Norfolk Naval Shipyard, attended the Naval Diving and Salvage Training Center and became a qualified Joint Diving Officer, served as Officer-in-Charge of Construction Dive Detachement Charlie and Assistant Operations Officer for Underwater Construction Team ONE, and was selected into the Ocean Facilities Program. Since January 2021, Justin has been a graduate student at the University of North Florida, in Jacksonville, Florida. Upon graduation Justin has follow on orders to the NAVFAC Engineering and Expeditionary Warfare Center in Port Hueneme, California.